Dynamic many-body theory: Multiparticle fluctuations and the dynamic structure of ^{4}He

C. E. Campbell,[1] E. Krotscheck,[2,3] and T. Lichtenegger[2,3]

[1]*School of Physics and Astronomy, University of Minnesota, Minneapolis, Minnesota 55455, USA*

[2]*Institut für Theoretische Physik, Johannes Kepler Universität, A 4040 Linz, Austria*

[3]*Department of Physics, University at Buffalo, SUNY Buffalo, New York 14260, USA*

(Received 23 February 2015; revised manuscript received 19 April 2015; published 14 May 2015)

We present further progress in a systematic approach to the microscopic understanding of the dynamics of strongly interacting quantum fluids. Employing the concept of dynamic multiparticle fluctuations, we derive equations of motion for fluctuating n-body densities. We apply the theory to calculate the dynamic structure function of liquid ^{4}He as a function of density and find, without any phenomenological input, overall excellent agreement with both experiments and, as far as available, simulation data.

DOI: 10.1103/PhysRevB.91.184510 PACS number(s): 05.30.Jp, 67.25.dt

I. INTRODUCTION

Much of our knowledge of the dynamics of strongly correlated quantum fluids, including liquid ^{4}He, is obtained from the liquid's dynamic structure function $S(\mathbf{k},\hbar\omega)$, which is directly measured by inelastic neutron scattering. In the linear-response regime, the double-differential cross section

$$\frac{\partial^2\sigma}{\partial\Omega\,\partial\hbar\omega} = b^2\left(\frac{k_1}{k_0}\right)S(\mathbf{k},\hbar\omega) \tag{1.1}$$

for this scattering is proportional to $S(\mathbf{k},\hbar\omega)$, where $\hbar\mathbf{k}$ and $\hbar\omega$ are the momentum and energy transferred to the system by the scattered neutron [1], Ω is the scattering solid angle, b is the scattering length of the nucleus, and $\hbar\mathbf{k}_0$ and $\hbar\mathbf{k}_1$ are the initial and final momenta of the scattered neutron. Reviews of the experimental, simulation, and theoretical results before 1994 for the liquid ^{4}He $S(\mathbf{k},\hbar\omega)$ are given in Refs. [2,3]. More recent results may be found in Refs. [4–18] and references cited therein.

In this paper, we report on an extension of our theory for the dynamics of a Bose quantum fluid and apply the theory to the dynamic structure function of liquid ^{4}He. We include *dynamic* pair [4] and triplet fluctuations using an equation-of-motion approach for correlated wave functions. This includes results for well-known features of the excitation spectrum of liquid ^{4}He measured by inelastic neutron scattering, e.g., the phonon, maxon, roton, and plateau features, illustrated in Fig. 1, as well as a "multiexcitation" continuum. We also reproduce fainter features of the dynamic structure function that have so far been found experimentally [8]. These are an extension of the phonon line into the continuum in the density regime of anomalous dispersion; a feature that can be identified as roton-maxon coupling; and an extension of the "Pitaevskii plateau" [19] to long wavelengths.

We also compare our theory with the formal results of a highly resummed version of Brillouin-Wigner perturbation theory (BW) for the lowest excited state using correlated basis functions [20,21].

More recently, much progress has been made in the development of simulation methods for dynamic quantities; see, e.g., Refs. [17,22]. These are very important algorithmic developments that will ultimately permit the very demanding elimination of background and multiple-scattering events from the raw data. The aim of our work is somewhat different: It is generally agreed upon that the model of static pair potentials such as the Aziz interaction describes the helium liquids accurately. Hence, given sufficiently elaborate algorithms and sufficient computing power, such calculations must reproduce the experimental data. The identification of different effects such as phonon-phonon, phonon-roton, roton-roton, maxon-roton,...couplings is only possible *a posteriori* whereas the semianalytic methods pursued here permit a direct identification of these effects and their physical mechanisms from the structure of the theory.

The well-known fact that the dynamic structure function couples to the excitation spectrum is clear from the zero-temperature relationship [23]

$$S(\mathbf{k},\hbar\omega) = \frac{1}{N}\sum_n |\langle\Psi_n|\rho_\mathbf{k}|\Psi_0\rangle|^2\delta(\hbar\omega-\varepsilon_n), \tag{1.2}$$

where the sum is over all of the fluid's eigenstates, $|\Psi_0\rangle$ is the (normalized) ground state of the N-particle system, and ε_n is the exact excitation energy of eigenstate $|\Psi_n\rangle$ (i.e., eigenvalue $E_n = E_0+\varepsilon_n$, where E_0 is the ground-state energy). $\rho_\mathbf{k}$ is the density fluctuation operator, which in coordinate representation is

$$\rho_\mathbf{k} \equiv \sum_{\ell=1}^{N}\exp(i\mathbf{k}\cdot\mathbf{r}_\ell), \tag{1.3}$$

where $\{\mathbf{r}_\ell\}$ are the coordinates of the N particles of the fluid. Thus, all excited states which have nonzero weight in the density fluctuation state $\rho_\mathbf{k}\Psi_0$ contribute to $S(\mathbf{k},\hbar\omega)$.

The earliest theory of the excitation spectrum, due to Feynman [24], is equivalent to a single resonance ansatz for $S(\mathbf{k},\hbar\omega)$:

$$\begin{aligned} S_0(\mathbf{k},\hbar\omega) &= \frac{1}{N}\left|\left\langle\Psi_\mathbf{k}^{(0)}\right|\rho_\mathbf{k}|\Psi_0\rangle\right|^2\delta[\hbar\omega-\varepsilon_0(\mathbf{k})] \\ &= S(\mathbf{k})\delta[\hbar\omega-\varepsilon_0(\mathbf{k})]. \end{aligned} \tag{1.4}$$

In this approximation, the only state in the sum is the Feynman state $\Psi_\mathbf{k}^{(0)} \equiv \rho_\mathbf{k}\Psi_0/\sqrt{NS(\mathbf{k})}$, which, however, is an exact eigenstate only in the long-wavelength limit. The corresponding excitation energy is the Bijl-Feynman energy

$$\varepsilon_0(\mathbf{k}) \equiv \frac{\hbar^2k^2}{2mS(\mathbf{k})}, \tag{1.5}$$

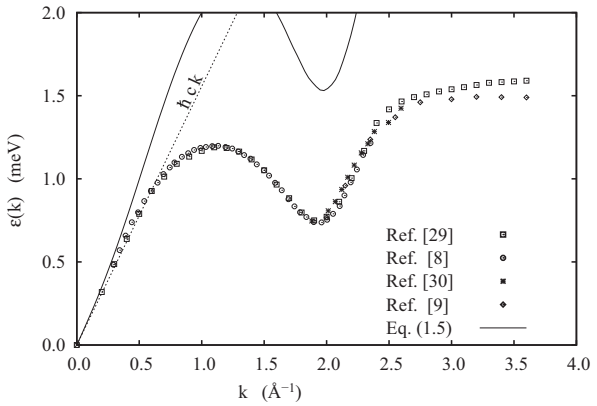

FIG. 1. The figure shows experimental data for the elementary excitations in ^{4}He at saturated vapor pressure (SVP): boxes from Ref. [29], circles from Ref. [8], stars from Ref. [30], and diamonds from Ref. [9]. Also shown is the Feynman spectrum $\varepsilon_0(k)$ [Eq. (1.5)] (solid line) and the phonon line $\hbar ck$, where c is the experimental speed of sound.

where m is the atomic mass, and $S(\mathbf{k})$ is the liquid structure factor

$$S(\mathbf{k}) = \frac{\langle \Psi_0 |\, \rho_{\mathbf{k}} \rho_{-\mathbf{k}} \,| \Psi_0 \rangle}{N}. \tag{1.6}$$

$S(\mathbf{k})$ has been independently measured using elastic neutron scattering and x-ray scattering [5,25–27]. In the Feynman approximation [Eqs. (1.4) and (1.5)], the excitation is undamped at all wave numbers.

It is well known that there is indeed a sharp elementary excitation spectrum $\varepsilon(k)$ measured in the dynamic structure function of liquid ^{4}He; this is shown in Fig. 1, where it is seen that $\varepsilon_0(k)$ is in quantitative agreement with the measured dispersion relationship $\varepsilon(k)$ at long wavelengths, i.e., in the phonon region. However, $\varepsilon_0(k)$ is only qualitatively correct at shorter wavelengths, including the maxon and roton regions, and fails even qualitatively in the higher-momentum "Pitaevskii plateau" [19] region.

It is customary to parametrize the dispersion relation of the collective mode in the vicinity of its minimum around $q \approx 2$ Å^{-1} (the *roton* minimum) as [28]

$$\varepsilon_{\mathrm{R}}(k) = \Delta_{\mathrm{R}} + \frac{\hbar^2}{2\mu_{\mathrm{R}}}(k - k_{\mathrm{R}})^2, \tag{1.7}$$

where Δ_{R} is the roton energy, k_{R} the wave number of the roton minimum, and μ_{R} the so-called roton mass. Moreover, there is a broad continuum in $S(k,\hbar\omega)$, at energies above $\varepsilon(k)$, which is generally attributed to multiexcitation contributions, not shown in Fig. 1. Accounting for these and other features of $S(\mathbf{k},\hbar\omega)$ has been the objective of much of the subsequent theoretical work, including the work that we present herein.

In most reports it has been found convenient to decompose the dynamic structure factor into a single pole term at $\hbar\omega = \varepsilon(k)$, and a continuum component S_m already found in the earliest experiments [29,31]:

$$S(\mathbf{k},\hbar\omega) = Z(\mathbf{k})\delta[\hbar\omega - \varepsilon(\mathbf{k})] + S_m(\mathbf{k},\hbar\omega). \tag{1.8}$$

$Z(\mathbf{k})$, the strength of the single excitation pole, is obviously less than or equal to $S(\mathbf{k})$, the difference being accounted for by the energy integral of $S_m(\mathbf{k},\hbar\omega)$. It has been observed that $Z(\mathbf{k})$ becomes negligible in the Pitaevskii plateau region above approximately 3.5 Å^{-1} for liquid ^{4}He at equilibrium density, and similarly at higher pressures [7,9].

In order to obtain the dynamic structure function from first principles, we have employed linear-response theory adapted for strongly correlated systems [4,32–34]. The dynamic response of the fluid's one-body density to a weak, time-dependent, external potential $\delta V_{\mathrm{ext}}(\mathbf{r},t)$ is expressed in terms of the dynamic density-density response function $\chi(\mathbf{r},\mathbf{r}';t)$ of the unperturbed fluid:

$$\delta\rho_1(\mathbf{r},t) = \int d^3r'dt'\ \chi(\mathbf{r},\mathbf{r}';t-t')\delta V_{\mathrm{ext}}(\mathbf{r}',t'), \tag{1.9}$$

where $\delta\rho_1(\mathbf{r},t)$ is the time-dependent part of the one-body density. The dynamic structure function is given by the imaginary part of frequency and wave-number Fourier transform of $\chi(\mathbf{r},\mathbf{r}';t)$:

$$S(\mathbf{k},\hbar\omega) = -\frac{1}{N\pi}\mathcal{I}m \int d^3r\, d^3r' e^{i\mathbf{k}\cdot(\mathbf{r}-\mathbf{r}')}\chi(\mathbf{r},\mathbf{r}';\hbar\omega). \tag{1.10}$$

[Here and elsewhere, it is most convenient to formally include the possibility that the density of the fluid is inhomogeneous, as we have in Eqs. (1.9) and (1.10).]

The equations of motion (EOM) for $\delta\rho_1(\mathbf{r},t)$ and other necessary multiparticle density fluctuations are obtained using the principle of least action [35,36]

$$\begin{aligned} 0 = \delta\mathcal{S} &= \delta\int_{t_1}^{t_2} dt\ \mathcal{L}(t) \\ &= \delta\int_{t_1}^{t_2} dt \langle\Psi(t)|H_0 + \delta H_{\mathrm{ext}}(t) - i\hbar\frac{\partial}{\partial t}|\Psi(t)\rangle, \end{aligned} \tag{1.11}$$

where $\mathcal{L}(t)$ is the Lagrangian,

$$\delta H_{\mathrm{ext}}(t) = \sum_i \delta V_{\mathrm{ext}}(\mathbf{r}_i;t) \tag{1.12}$$

is a small, time-dependent perturbation, and $|\Psi(t)\rangle$ is the perturbed wave function. The latter can be written in complete generality as

$$|\Psi(t)\rangle = \frac{e^{-iE_0t/\hbar}\, e^{\frac{1}{2}\delta U(t)}|\Psi_0\rangle}{[\langle\Psi_0|e^{\mathcal{R}e\,\delta U(t)}|\Psi_0\rangle]^{1/2}}, \tag{1.13}$$

where E_0 is the ground-state energy, and $\delta U(t)$ is the complex *excitation operator*. In coordinate representation, it is convenient to express this excitation operator as a time-dependent Feenberg function

$$\begin{aligned} \delta U(t) &= \sum_i \delta u_1(\mathbf{r}_i;t) + \sum_{i<j}\delta u_2(\mathbf{r}_i,\mathbf{r}_j;t) + \cdots \\ &\equiv \delta U_1(t) + \delta U_2(t) + \cdots, \end{aligned} \tag{1.14}$$

where the sums in the first line are over all of the particles.

The Feynman approximation is obtained by including only $\delta U_1(t)$ in the excitation operator, i.e., $\delta U_n(t) = 0$ for $n \geqslant 2$ [32]. Significant improvement was achieved by also including dynamic two-body fluctuations $\delta U_2(t)$ [4,33,34,37]. For fermions, the restriction of $U(t)$ to one-body fluctuations

leads to a generalization of the time-dependent Hartree-Fock approximation to strongly interacting systems [38,39], similarly the inclusion of pair excitations provides a significant improvement of the agreement between theory and experiment [40,41]. In this work, we extend this theory to include dynamic three-body fluctuations by simultaneously determining $\delta U_n(t)$, $n = 1,2,3$, achieving excellent agreement with experimental results extrapolated to zero temperature.

The concept of dynamic multiparticle fluctuations has been discussed in the past in various places; see, for example, Ref. [42]. At the level of dynamic pair fluctuations, the most complete solution of the equations of motion, which involved a solution of the full, linearized hypernetted chain Euler-Lagrange equations (HNC-EL) for the pair fluctuations, has been presented as the first paper of this series [4]. However, in that work it was found that such a fully self-consistent calculation does not lead to a significant improvement of the excitation spectrum over that obtained with the relatively simple convolution approximation [43–46].

To proceed with the inclusion of dynamical three-particle fluctuations, it is necessary to have accurate information about the ground-state wave function in the form of its multiparticle density functions $\rho_n(\mathbf{r}_1,\ldots\mathbf{r}_n)$:

$$\rho_n(\mathbf{r}_1,\ldots,\mathbf{r}_n) = \frac{N!}{(N-n)!}\frac{\int d^3r_{n+1}\ldots d^3r_N|\Psi_0(\mathbf{r}_1,\ldots,\mathbf{r}_N)|^2}{\int d^3r_1\ldots d^3r_N|\Psi_0(\mathbf{r}_1,\ldots,\mathbf{r}_N)|^2} \quad (1.15)$$

and the corresponding dimensionless multiparticle distribution functions

$$g_n(\mathbf{r}_1,\ldots,\mathbf{r}_n) = \frac{\rho_n(\mathbf{r}_1,\ldots,\mathbf{r}_n)}{\rho_1(\mathbf{r}_1)\ldots\rho_1(\mathbf{r}_n)} \quad (1.16)$$

for $n = 1,\ldots,5$.

While information about the ground-state wave function of liquid ^{4}He, including some low-order distribution functions, is available from quantum Monte Carlo simulations, presently it seems not to be possible to extract sufficiently high-order correlation functions with sufficient accuracy for the implementation of our theory. However, functional variation methods, such as the Feenberg-Jastrow-Euler-Lagrange (FJEL) theory, have been developed over the past three decades to a level where the quantitative prediction of ground-state properties of strongly interacting bulk Bose liquids is a routine matter [39].

The FJEL theory for the ground state of a strongly interacting system of N identical bosons conventionally begins with an empirical Hamiltonian

$$H_0 = \sum_{i=1}^{N}\left\{-\frac{\hbar^2}{2m}\nabla_i^2 + V_1(\mathbf{r}_i)\right\} + \sum_{1\leqslant i<j\leqslant N} V_2(|\mathbf{r}_i-\mathbf{r}_j|), \quad (1.17)$$

where $V_1(\mathbf{r})$ is an external potential, and $V_2(|\mathbf{r}_i-\mathbf{r}_j|)$ is the two-particle interaction. The strong, short-ranged repulsion in $V_2(|\mathbf{r}_i-\mathbf{r}_j|)$ is readily dealt with in the FJEL theory. The ground-state wave function for a system of N identical bosons with coordinates $\mathbf{r}_1,\ldots,\mathbf{r}_N$ is written in the Feenberg form [47–49]

$$\Psi_0(\mathbf{r}_1,\ldots,\mathbf{r}_N) = \mathcal{N}^{-1/2}\exp\frac{1}{2}\left\{\sum_i u_1(\mathbf{r}_i) + \sum_{i<j} u_2(\mathbf{r}_i,\mathbf{r}_j) + \cdots\right\}, \quad (1.18)$$

where $\mathcal{N}$ is the normalization integral, and the static correlation functions $u_n(\mathbf{r}_1,\ldots,\mathbf{r}_n)$ are real and symmetric under particle exchange. These functions may be obtained by simultaneously solving the set of Euler-Lagrange (EL) equations that minimize the energy expectation value E_0 [47,50–53]:

$$\frac{\delta E_0}{\delta u_n(\mathbf{r}_1,\ldots,\mathbf{r_n})} = 0, \quad (1.19)$$

where

$$E_0 = \langle\Psi_0|\,H_0\,|\Psi_0\rangle. \quad (1.20)$$

If all N of these EL equations were solved, Ψ_0 would be the exact ground state and E_0 the exact ground-state energy. This is, of course, impractical; however, it has proven unnecessary to go beyond $n = 3$ to obtain excellent agreement with experiments for bulk liquid ^{4}He as well as inhomogeneous systems such as adsorbed films [54–56]. The one-body function $u_1(\mathbf{r}_i)$ determines the spatial structure of the system, and the two-body function $u_2(\mathbf{r}_i,\mathbf{r}_j)$ describes the short- and long-range correlations between pairs of particles. Triplet correlations in the form of $u_3(\mathbf{r}_i,\mathbf{r}_j,\mathbf{r}_k)$ are needed to provide quantitative agreement between theoretical predictions and the very low-temperature experimental equation of state [47,52,53]. Three-body correlations contribute visibly to the nearest-neighbor peak of the pair distribution function $g_2(\mathbf{r}_i,\mathbf{r}_j)$, the maximum of the liquid structure factor, and the density dependence of the roton [46].

In the following, we detail our theory of $S(\mathbf{k},\hbar\omega)$ including dynamic three-body fluctuations. In Sec. II, we formulate the general concept of dynamic multiparticle fluctuations and derive relationships for the fluctuating densities and currents. A key aspect of this analysis is a transformation to a more convenient set of independent functional variables. Section III derives the Lagrangian and brings it into a form that is suitable for deriving the equations of motion. The general equations of motion are derived in Sec. IV and, from these, the density-density response function. In that section, we will utilize the convolution approximation [43,57,58] to formulate a compact and practical theory. Some of the more technical aspects of our derivations are contained in the Appendices.

An alternative approach to the theory of the excitation spectrum that has been utilized in the past [20,43–46] is Brillouin-Wigner (BW) perturbation theory in a correlated basis. We discuss the relationship of the EOM method and the BW expansion in Sec. V. The BW expansion will provide justification for some of the generalizations of our working formulas which would be very tedious to derive from multiparticle fluctuations. In turn, the EOM method provides justification for generalizing the BW working formulas, which are, strictly speaking valid only for the lowest-lying excitation, to the full density-density response function.

The concluding Sec. VI first discusses a sequence of comparisons of our ground-state results with experiments and simulation data. We then present results on generic properties of the excitation spectrum: the strength (1.8) of the single-phonon pole, the energy, momentum, and effective mass of the roton excitation, and the static density-density response function. A very useful reference on this point is the compilation of experimental and simulation data of Caupin *et al.* [5]. We then proceed to discuss our results for the dynamic structure function $S(\mathbf{k},\hbar\omega)$ in the fluid density regime between $\rho = 0.021$ and $0.025\,\text{Å}^{-3}$ and mention some finer details that might be experimentally visible. We conclude by briefly discussing high-lying excitations.

II. MULTIPARTICLE FLUCTUATIONS

A. Fluctuating densities and distribution functions

The time-dependent parts of the correlations $\delta u_n(\mathbf{r}_1,\ldots,\mathbf{r}_n;t)$ are determined by the action principle (1.11). Expanding the Lagrangian to second order leads to [4]

$$\begin{aligned}\mathcal{L}(t) &= \tfrac{1}{8}\{\langle\Psi_0|[\delta U^*,[T,\delta U]]|\Psi_0\rangle \\ &\quad -i\hbar\langle\Psi_0|[\delta\dot{U}\delta U^* - \text{c.c.}]|\Psi_0\rangle\} \\ &\quad + \tfrac{1}{2}\langle\Psi_0|[\delta U^*(t)\delta H_{\text{ext}}(t) + \delta H_{\text{ext}}(t)\delta U(t)]|\Psi_0\rangle \\ &= \mathcal{L}_{\text{int}}(t) + \mathcal{L}_t(t) + \mathcal{L}_{\text{ext}}(t), \end{aligned} \tag{2.1}$$

where $|\Psi_0\rangle$ is normalized, and it has been assumed, without loss of generality, that the fluctuating part of the wave function is orthogonal to the ground state: $\langle\Psi_0|\delta U(t)|\Psi_0\rangle = 0$.

In this section, we consider a truncated form of the excitation operator (1.14) that includes up to three-body fluctuations. Central quantities for the description of the physics are fluctuations of the n-body densities corresponding to the above wave function. It is convenient and useful for the definitions of these fluctuations and the one-particle current to be generalized *complex functions,* where the physical fluctuations are their real parts.

Formally we make no assumptions yet about specific symmetries such as translational invariance or isotropy; in cases where one has to deal with multiparticle densities, such assumptions provide practically no formal simplifications.

The complex fluctuations $\delta u_n(\mathbf{r}_1,\ldots,\mathbf{r}_n;t)$ induce a time dependence of the n-body densities (1.15). We can generally write the time-dependent parts of the densities in terms of functional variations of the ground-state densities (1.15) with respect to the correlation amplitudes $u_n(\mathbf{r}_1,\ldots,\mathbf{r}_n)$ and the fluctuations $\delta u_n(\mathbf{r}_1,\ldots,\mathbf{r}_n;t)$. When doing these variations, it is useful to take the $u_n(\mathbf{r}_1,\ldots,\mathbf{r}_n)$ as independent functions, subsequently evaluating them at their optimal ground-state forms. For example, the time-dependent part of the one-body density is

$$\begin{aligned}\delta\rho_1(\mathbf{r};t) &= \int d^3r_1 \frac{\delta\rho_1(\mathbf{r})}{\delta u_1(\mathbf{r}_1)}\delta u_1(\mathbf{r}_1;t) \\ &\quad + \int d^3r_1 d^3r_2 \frac{\delta\rho_1(\mathbf{r})}{\delta u_2(\mathbf{r}_1,\mathbf{r}_2)}\delta u_2(\mathbf{r}_1,\mathbf{r}_2;t) \\ &\quad + \int d^3r_1 d^3r_2 d^3r_3 \frac{\delta\rho_1(\mathbf{r})}{\delta u_3(\mathbf{r}_1,\mathbf{r}_2,\mathbf{r}_3)}\,\delta u_3(\mathbf{r}_1,\mathbf{r}_2,\mathbf{r}_3;t), \end{aligned} \tag{2.2}$$

where $\rho_1(\mathbf{r})$ is a functional of the set of real functions $\{u_n\}$ but *not* a functional of $\{\delta u_n\,,\delta u_n^*\}$. The physical one-body density fluctuation is the real part of Eq. (2.2) and thus contains both δu_n and δu_n^*.

Using the symmetry

$$\frac{\delta\rho_1(\mathbf{r})}{\delta u_n(\mathbf{r}_1,\ldots,\mathbf{r}_n)} = \frac{1}{n!}\frac{\delta\rho_n(\mathbf{r}_1,\ldots,\mathbf{r}_n)}{\delta u_1(\mathbf{r})}, \tag{2.3}$$

we can rewrite Eq. (2.2) as

$$\begin{aligned}\delta\rho_1(\mathbf{r};t) &= \int d^3r_1 \frac{\delta\rho_1(\mathbf{r}_1)}{\delta u_1(\mathbf{r})}\,\delta u_1(\mathbf{r}_1;t) \\ &\quad + \frac{1}{2!}\int d^3r_1 d^3r_2 \frac{\delta\rho_2(\mathbf{r}_1,\mathbf{r}_2)}{\delta u_1(\mathbf{r})}\,\delta u_2(\mathbf{r}_1,\mathbf{r}_2;t) \\ &\quad + \frac{1}{3!}\int d^3r_1 d^3r_2 d^3r_3 \frac{\delta\rho_3(\mathbf{r}_1,\mathbf{r}_2,\mathbf{r}_3)}{\delta u_1(\mathbf{r})}\,\delta u_3(\mathbf{r}_1,\mathbf{r}_2,\mathbf{r}_3;t) \\ &\quad . \end{aligned} \tag{2.4}$$

A key step in the derivation of the equations of motion is to introduce a new set of independent dynamical variables $\delta v_n(\mathbf{r}_1,\ldots,\mathbf{r}_n;t)$ in the action principle (1.11). The one-body function $\delta v_1(\mathbf{r}_1;t)$ is defined by

$$\begin{aligned}\delta\rho_1(\mathbf{r};t) &\equiv \int d^3r' \frac{\delta\rho_1(\mathbf{r})}{\delta u_1(\mathbf{r}')}\,\delta v_1(\mathbf{r}';t) \\ &= \int d^3r' \frac{\delta\rho_1(\mathbf{r}')}{\delta u_1(\mathbf{r})}\,\delta v_1(\mathbf{r}';t), \end{aligned} \tag{2.5}$$

where

$$\begin{aligned}\frac{\delta\rho_1(\mathbf{r})}{\delta u_1(\mathbf{r}')} &= \rho_1(\mathbf{r})\delta(\mathbf{r}-\mathbf{r}') + \rho_2(\mathbf{r},\mathbf{r}') - \rho_1(\mathbf{r})\rho_1(\mathbf{r}') \\ &\equiv \rho_1(\mathbf{r})S(\mathbf{r},\mathbf{r}')\rho_1(\mathbf{r}') \end{aligned} \tag{2.6}$$

and $S(\mathbf{r},\mathbf{r}')$ is the coordinate representation of the static structure function.

From Eq. (2.4) we find the relationship between $\delta u_1(\mathbf{r};t)$ and $\delta v_1(\mathbf{r};t)$:

$$\begin{aligned}\delta v_1(\mathbf{r};t) &= \delta u_1(\mathbf{r};t) + \int d^3r' \frac{\delta u_1(\mathbf{r}')}{\delta\rho_1(\mathbf{r})}\left[\frac{1}{2!}\int d^3r_1 d^3r_2 \frac{\delta\rho_2(\mathbf{r}_1,\mathbf{r}_2)}{\delta u_1(\mathbf{r}')}\delta u_2(\mathbf{r}_1,\mathbf{r}_2;t) + \frac{1}{3!}\int d^3r_1 d^3r_2 d^3r_3 \frac{\delta\rho_3(\mathbf{r}_1,\mathbf{r}_2,\mathbf{r}_3)}{\delta u_1(\mathbf{r}')}\delta u_3(\mathbf{r}_1,\mathbf{r}_2,\mathbf{r}_3;t)\right] \\ &= \delta u_1(\mathbf{r};t) + \frac{1}{2!}\int d^3r_1 d^3r_2 \frac{\delta\rho_2(\mathbf{r}_1,\mathbf{r}_2)}{\delta\rho_1(\mathbf{r})}\delta u_2(\mathbf{r}_1,\mathbf{r}_2;t) + \frac{1}{3!}\int d^3r_1 d^3r_2 d^3r_3 \frac{\delta\rho_3(\mathbf{r}_1,\mathbf{r}_2,\mathbf{r}_3)}{\delta\rho_1(\mathbf{r})}\delta u_3(\mathbf{r}_1,\mathbf{r}_2,\mathbf{r}_3;t). \end{aligned} \tag{2.7}$$

How the variation with respect to the one-body density is done must be explained. *A priori,* the two-body density and/or pair distribution function can be expressed as a diagrammatic expansion in terms of n-body correlation functions $u_n(\mathbf{r}_1,\ldots,\mathbf{r}_n)$, the fundamental diagrammatic elements being e^{u_1} and, for $n>1$, $e^{u_n}-1$. These diagrams contain *articulation points.* Diagrams containing such articulation points are called *point reducible.* These reducible diagrams can all be eliminated by re-interpreting each point as a density factor $\rho_1(\mathbf{r}_i)$; therefore, we may think of $\rho_2(\mathbf{r}_1,\mathbf{r}_2)$ and $\rho_3(\mathbf{r}_1,\mathbf{r}_2,\mathbf{r}_3)$ also as expansions in terms of the one-body density $\rho_1(\mathbf{r}_i)$ and pair and triplet correlations $u_2(\mathbf{r}_i,\mathbf{r}_j)$ and $u_3(\mathbf{r}_i,\mathbf{r}_j,\mathbf{r}_k)$. These expansions are represented by the same sets of diagrams as before, with the additional *dictum* that they contain no point-reducible diagrams, and individual points are interpreted as carrying a factor $\rho_1(\mathbf{r}_i)$ instead of $e^{u_1(\mathbf{r}_i)}$. The variation with respect to the density is done on these expansions.

As in Ref. [4], we use $\delta v_1(\mathbf{r};t)$ as an independent one-body function in the action principle (1.11). However, since there is a one-to-one relationship between $\delta v_1(\mathbf{r};t)$ and $\delta\rho_1(\mathbf{r};t)$, this is the same as keeping the latter as the independent one-body function.

Operationally, one proceeds for the two-body fluctuations as follows: The point-reducible diagrams contributing to $g_2(\mathbf{r}_1,\mathbf{r}_2)$ can again be summed to give the density factors $\rho_1(\mathbf{r}_i)$ at each diagram point $\mathbf{r}_i$. Consequently, we can consider the pair distribution function as a functional of the one-body density $\rho_1(\mathbf{r}_i)$ and pair and triplet correlations $u_2(\mathbf{r}_i,\mathbf{r}_j)$ and $u_3(\mathbf{r}_i,\mathbf{r}_j,\mathbf{r}_k)$. The time-dependent part is then, to linear order,

$$\begin{aligned}
&\delta g_2(\mathbf{r}_1,\mathbf{r}_2;t)\\
&\quad=\int d^3r_1'\frac{\delta g_2(\mathbf{r}_1,\mathbf{r}_2)}{\delta\rho_1(\mathbf{r}_1')}\delta\rho_1(\mathbf{r}_1';t)\\
&\qquad+\int d^3r_1'd^3r_2'\frac{\delta g_2(\mathbf{r}_1,\mathbf{r}_2)}{\delta u_2(\mathbf{r}_1',\mathbf{r}_2')}\delta u_2(\mathbf{r}_1',\mathbf{r}_2';t)\\
&\qquad+\int d^3r_1'd^3r_2'd^3r_3'\frac{\delta g_2(\mathbf{r}_1,\mathbf{r}_2)}{\delta u_3(\mathbf{r}_1',\mathbf{r}_2',\mathbf{r}_3')}\delta u_3(\mathbf{r}_1',\mathbf{r}_2',\mathbf{r}_3';t)\\
&\quad\equiv\int d^3r_1'\frac{\delta g_2(\mathbf{r}_1,\mathbf{r}_2)}{\delta\rho_1(\mathbf{r}_1')}\delta\rho_1(\mathbf{r}_1';t)\\
&\qquad+\int d^3r_1'd^3r_2'\frac{\delta g_2(\mathbf{r}_1,\mathbf{r}_2)}{\delta u_2(\mathbf{r}_1',\mathbf{r}_2')}\delta v_2(\mathbf{r}_1',\mathbf{r}_2';t).
\end{aligned}\tag{2.8}$$

The last line defines $\delta v_2(\mathbf{r}_1,\mathbf{r}_2;t)$. For a consistent notation we shall also identify $\delta v_3(\mathbf{r}_1,\mathbf{r}_2,\mathbf{r}_3;t)\equiv\delta u_3(\mathbf{r}_1,\mathbf{r}_2,\mathbf{r}_3;t)$.

To proceed further, we can make use of symmetry relations for the functional derivatives of g_n similar to those for ρ_n [Eq. (2.3)]. These are obtained by first noting that the logarithm of the ground-state normalization integral $\ln\mathcal{N}$, defined by Eq. (1.18), is a functional of the set of the static correlation functions $\{u_n\}$, which may be used as the generator of the ground-state distribution functions ρ_n by functional differentiation with respect to u_n. The symmetry relations for the functional derivatives of the n-body densities given in Eq. (2.3) is due to the commutativity of the second functional cross derivatives of $\ln\mathcal{N}$ with respect to $\{u_n\}$ and $\{u_m\}$ with $n\neq m$. The corresponding symmetry relations for the dimensionless distribution functions g_n [Eq. (1.16)] are obtained by a functional Legendre transformation of $\ln\mathcal{N}$ to a new generating functional of the functions $\{\rho_1,u_2,u_3,\ldots\}$. The equality of the second cross derivatives of this generating functional, together with the definition of the multiparticle distribution functions (1.16), gives the desired symmetry relations

$$\begin{aligned}
&\rho_1(\mathbf{r}_1)\rho_1(\mathbf{r}_2)\frac{\delta g_2(\mathbf{r}_1,\mathbf{r}_2)}{\delta u_2(\mathbf{r}_1',\mathbf{r}_2')}\\
&\quad=\rho_1(\mathbf{r}_1')\rho_1(\mathbf{r}_2')\frac{\delta g_2(\mathbf{r}_1',\mathbf{r}_2')}{\delta u_2(\mathbf{r}_1,\mathbf{r}_2)},\\
&\rho_1(\mathbf{r}_1)\rho_1(\mathbf{r}_2)\frac{\delta g_2(\mathbf{r}_1,\mathbf{r}_2)}{\delta u_3(\mathbf{r}_1',\mathbf{r}_2',\mathbf{r}_3')}\\
&\quad=\frac{2!}{3!}\rho_1(\mathbf{r}_1')\rho_1(\mathbf{r}_2')\rho_1(\mathbf{r}_3')\frac{\delta g_3(\mathbf{r}_1',\mathbf{r}_2',\mathbf{r}_3')}{\delta u_2(\mathbf{r}_1,\mathbf{r}_2)}.
\end{aligned}\tag{2.9}$$

As in the transition from Eqs. (2.2) to (2.4), we use these symmetry relations to solve for $\delta v_2(\mathbf{r}_1,\mathbf{r}_2;t)$:

$$\begin{aligned}
\delta v_2(\mathbf{r}_1,\mathbf{r}_2;t)&=\delta u_2(\mathbf{r}_1,\mathbf{r}_2;t)\\
&\quad+\int d^3\rho_1'd^3\rho_2'd^3\rho_3'\mathcal{G}_{23}(\mathbf{r}_1,\mathbf{r}_2;\mathbf{r}_1',\mathbf{r}_2',\mathbf{r}_3')\\
&\quad\times\delta u_3(\mathbf{r}_1',\mathbf{r}_2',\mathbf{r}_3';t),
\end{aligned}\tag{2.10}$$

where

$$\mathcal{G}_{23}(\mathbf{r}_1,\mathbf{r}_2;\mathbf{r}_1',\mathbf{r}_2',\mathbf{r}_3')\equiv\frac{1}{3\rho_1(\mathbf{r}_1)\rho_1(\mathbf{r}_2)}\frac{\delta g_3(\mathbf{r}_1',\mathbf{r}_2',\mathbf{r}_3')}{\delta g_2(\mathbf{r}_1,\mathbf{r}_2)}\tag{2.11}$$

and we have introduced the notation $d^3\rho_i\equiv\rho_1(\mathbf{r}_i)d^3r_i$. We will also use the notation $\mathcal{G}_{32}(\mathbf{r}_1',\mathbf{r}_2',\mathbf{r}_3';\mathbf{r}_1,\mathbf{r}_2)\equiv\mathcal{G}_{23}(\mathbf{r}_1,\mathbf{r}_2;\mathbf{r}_1',\mathbf{r}_2',\mathbf{r}_3')$ to specify the order of the coefficients. We must again specify how the variation of $g_3(\mathbf{r}_1',\mathbf{r}_2',\mathbf{r}_3')$ with respect to $g_2(\mathbf{r}_1,\mathbf{r}_2)$ is done: One first derives a diagrammatic expansion in terms $\rho_1(\mathbf{r}_i)$ and $u_n(\mathbf{r}_1,\ldots,\mathbf{r}_n)$ ($n\geqslant 2$). Then, one identifies all diagrams that can be separated from the rest by cutting two points. Reinterpreting the single line as $h_2(\mathbf{r}_i,\mathbf{r}_j)\equiv g_2(\mathbf{r}_i,\mathbf{r}_j)-1$, one can now rewrite the expansion for $g_3(\mathbf{r}_1',\mathbf{r}_2',\mathbf{r}_3')$ as a functional of $g_2(\mathbf{r}_i,\mathbf{r}_j)$, $\rho_1(\mathbf{r}_i)$, and $u_3(\mathbf{r}_i,\mathbf{r}_j,\mathbf{r}_k)$ (Abe expansion [59]). The procedure is the same as going from "elementary" to "basic" diagrams in the hypernetted theory (HNC) of classical fluids [60]. The variation with respect to $g_2(\mathbf{r}_1,\mathbf{r}_2)$ is then derived from this expansion.

B. One-body current

For the one-body equation, we need to express the expectation value of the one-body current operator in terms of the new variables $\delta v_n(\mathbf{r}_1,\ldots,\mathbf{r}_n;t)$. Beginning with

$$\begin{aligned}
\mathbf{j}(\mathbf{r};t)=\frac{\hbar}{2mi}\Big[&\rho_1(\mathbf{r})\nabla\delta u_1(\mathbf{r};t)+\int d^3r_1\rho_2(\mathbf{r},\mathbf{r}_1)\nabla_{\mathbf{r}}\delta u_2(\mathbf{r},\mathbf{r}_1;t)\\
&+\frac{1}{2}\int d^3r_1d^3r_2\rho_3(\mathbf{r},\mathbf{r}_1,\mathbf{r}_2)\nabla_{\mathbf{r}}\delta u_3(\mathbf{r},\mathbf{r}_1,\mathbf{r}_2;t)\Big],
\end{aligned}\tag{2.12}$$

we eliminate the $\delta u_1(\mathbf{r};t)$ and $\delta u_2(\mathbf{r},\mathbf{r}';t)$ in favor of $\delta v_1(\mathbf{r};t)$ and $\delta v_2(\mathbf{r},\mathbf{r}';t)$, using Eqs. (2.7) and (2.10):

$$\mathbf{j}(\mathbf{r};t) = \frac{\hbar}{2mi}\rho_1(\mathbf{r})\Big[\nabla\delta v_1(\mathbf{r};t) - \frac{1}{2}\int d^3\rho_1 d^3\rho_2 \mathbf{W}_2(\mathbf{r};\mathbf{r}_1,\mathbf{r}_2)\delta v_2(\mathbf{r}_1,\mathbf{r}_2;t) - \frac{1}{3!}\int d^3\rho_1 d^3\rho_2 d^3\rho_3 \mathbf{W}_3(\mathbf{r};\mathbf{r}_1,\mathbf{r}_2,\mathbf{r}_3) \times \delta v_3(\mathbf{r}_1,\mathbf{r}_2,\mathbf{r}_3;t)\Big], \tag{2.13}$$

where

$$\mathbf{W}_2(\mathbf{r};\mathbf{r}_1,\mathbf{r}_2) \equiv \frac{\delta(\mathbf{r}_1-\mathbf{r})}{\rho_1(\mathbf{r})}\nabla_{\mathbf{r}} g_2(\mathbf{r},\mathbf{r}_2) + \frac{\delta(\mathbf{r}_2-\mathbf{r})}{\rho_1(\mathbf{r})}\nabla_{\mathbf{r}} g_2(\mathbf{r}_1,\mathbf{r}) + \nabla_{\mathbf{r}}\frac{\delta g_2(\mathbf{r}_1,\mathbf{r}_2)}{\delta\rho_1(\mathbf{r})} \tag{2.14}$$

and

$$\mathbf{W}_3(\mathbf{r};\mathbf{r}_1,\mathbf{r}_2,\mathbf{r}_3) \equiv \frac{\delta(\mathbf{r}_1-\mathbf{r})}{\rho_1(\mathbf{r})}\nabla_{\mathbf{r}} g_3(\mathbf{r},\mathbf{r}_2,\mathbf{r}_3) + \text{cycl.} - \frac{2}{\rho_1(\mathbf{r})}\int d^3r' \nabla_{\mathbf{r}} g_2(\mathbf{r},\mathbf{r}')\frac{\delta g_3(\mathbf{r}_1,\mathbf{r}_2,\mathbf{r}_3)}{\delta g_2(\mathbf{r},\mathbf{r}')} + \nabla_{\mathbf{r}}\frac{\delta g_3(\mathbf{r}_1,\mathbf{r}_2,\mathbf{r}_3)}{\delta\rho_1(\mathbf{r})}\Big|_{g_2(\mathbf{r},\mathbf{r}')}. \tag{2.15}$$

We will show in Appendix A1 that $\mathbf{W}_3(\mathbf{r};\mathbf{r}_1,\mathbf{r}_2,\mathbf{r}_3)$ *vanishes for a Jastrow wave function.* The current then assumes the simple form

$$\mathbf{j}(\mathbf{r};t) = \frac{\hbar}{2mi}\rho_1(\mathbf{r})\Big[\nabla_{\mathbf{r}}\delta v_1(\mathbf{r};t) - \frac{1}{2}\int d^3\rho_1 d^3\rho_2 \mathbf{W}_2(\mathbf{r};\mathbf{r}_1,\mathbf{r}_2)\delta v_2(\mathbf{r}_1,\mathbf{r}_2;t)\Big] \tag{2.16}$$

$$\equiv \mathbf{j}_F(\mathbf{r};t) + \mathbf{j}_p(\mathbf{r};t). \tag{2.17}$$

In an obvious decomposition, Eqs. (2.16) and (2.17) define a "Feynman current" $\mathbf{j}_F(\mathbf{r};t)$ and a "pair induced current" $\mathbf{j}_p(\mathbf{r};t)$. The name "Feynman current" indicates that this term survives in the Feynman approximation $\delta u_2(\mathbf{r}_1,\mathbf{r}_2;t) = 0$. Note again that we have defined $\mathbf{j}_F(\mathbf{r};t)$ and $\mathbf{j}_p(\mathbf{r};t)$ as *complex* quantities; the real part of $\mathbf{j}$ is the physical one-body current.

Although triplet correlations are routinely included in ground-state calculations, we will neglect these effects in order to simplify the further analysis; i.e., we shall from here on use Eqs. (2.16) and (2.14) for the current.

III. LAGRANGIAN

The individual terms of the Lagrangian (2.1) have been derived in many places; see, for example, Refs. [4,42]. We only need to spell out the changes due to our new choice of independent variables and the inclusion of three-body fluctuations.

A. External field term

The term involving the external potential is, to first order in the fluctuations,

$$\mathcal{L}_{\text{ext}}(t) = \langle\Psi_0|\sum_i \delta V_{\text{ext}}(\mathbf{r}_i;t)|\Psi_0\rangle = \int d^3r\, \delta V_{\text{ext}}(\mathbf{r};t)\delta\rho_1(\mathbf{r};t). \tag{3.1}$$

In our choice of independent functions, this term is simply

$$\mathcal{L}_{\text{ext}}(t) = \frac{1}{2}\int d^3r\, d^3r'\, \delta V_{\text{ext}}(\mathbf{r})\frac{\delta\rho_1(\mathbf{r})}{\delta u_1(\mathbf{r}')}[\delta v_1(\mathbf{r}';t) + \delta v_1^*(\mathbf{r}';t)]. \tag{3.2}$$

B. Time-derivative term

For the time-derivative term in the action integral (1.11), we obtain, through second order in $\delta U(t)$,

$$\mathcal{L}_t(t) = -\frac{i\hbar}{8}[\langle\Psi_0|\delta\dot{U}\delta U^*|\Psi_0\rangle - \text{c.c.}]. \tag{3.3}$$

Because of the relation

$$\frac{\delta\mathcal{L}_t(t)}{\delta u_n^*(\mathbf{r}_1,\ldots,\mathbf{r}_n;t)} = -\frac{i\hbar}{8n!}\delta\dot{\rho}_n(\mathbf{r}_1,\ldots,\mathbf{r}_n;t), \tag{3.4}$$

we have

$$\mathcal{L}_t(t) = -\frac{i\hbar}{8}\sum_n\frac{1}{n!}\int d^3r_1\ldots d^3r_n[\delta\dot{\rho}_n(\mathbf{r}_1,\ldots,\mathbf{r}_n;t) \times \delta u_n^*(\mathbf{r}_1,\ldots,\mathbf{r}_n;t) - \text{c.c.}]. \tag{3.5}$$

Working with the fluctuations $\delta u_n(\mathbf{r}_1,\ldots,\mathbf{r}_n;t)$, one would now have to expand the $\delta\dot{\rho}_n(\mathbf{r}_1,\ldots,\mathbf{r}_n;t)$ in terms of ground-state densities and one-, two-, and three-body fluctuations. For three-body fluctuations, this can lead to up to six-body distribution functions. The expression for $\mathcal{L}_t(t)$ is considerably simplified by rewriting it in terms of the new variables $\delta v_1(\mathbf{r};t)$, $\delta v_2(\mathbf{r}_i,\mathbf{r}_j;t)$, and $\delta v_3(\mathbf{r}_i,\mathbf{r}_j,\mathbf{r}_k;t)$. The relevant derivations are carried out in Appendix A2; we can summarize our results as

$$\frac{\delta\mathcal{L}_t(t)}{\delta v_n^*(\mathbf{r}_1,\ldots,\mathbf{r}_n;t)} = -\frac{i\hbar}{4n!}\int d^3r_1'\ldots d^3r_n'\frac{\delta\rho_n(\mathbf{r}_1,\ldots,\mathbf{r}_n)}{\delta u_n(\mathbf{r}_1',\ldots,\mathbf{r}_n')}\delta\dot{v}_n(\mathbf{r}_1',\ldots,\mathbf{r}_n';t). \tag{3.6}$$

The two expressions (3.2) and (3.6), together with the result of Sec. II B that, for a Jastrow wave function, the one-body current $\mathbf{j}(\mathbf{r};t)$ has the form (2.17) *even if fluctuating triplet correlations are included*, are the key reason for introducing the new variables $\delta v_n(\mathbf{r}_1,\ldots,\mathbf{r}_n;t)$.

C. Interaction Lagrangian

The interaction Lagrangian requires the largest amount of work. We evaluate this term in three steps: The first step is to calculate directly $\mathcal{L}_{\text{int}}(t)$ from Eq. (3.7). In the second step, we eliminate $\delta u_1(\mathbf{r}_i;t)$ in favor of $\delta v_1(\mathbf{r}_i;t)$ using Eq. (2.7), and in the third, we also eliminate $\delta u_2(\mathbf{r}_i,\mathbf{r}_j;t)$ using Eq. (2.10).

Generally, we can write

$$\mathcal{L}_{\rm int}(t) = \frac{1}{8}\langle\Psi_0|[\delta U^*,[T,\delta U]]|\Psi_0\rangle = \sum_{i,j=1}^{3}\mathcal{L}_{\rm int}^{(ij)}(t), \quad (3.7)$$

where the $\mathcal{L}_{\rm int}^{(ij)}(t)$ contains one i-body fluctuation and one j-body fluctuation and $\mathcal{L}_{\rm int}^{(ij)}(t) = \mathcal{L}_{\rm int}^{*(ji)}(t)$. The general form of these terms is

$$\mathcal{L}_{\rm int}^{(ij)}(t) = \frac{\hbar^2}{8m}\int d^3\rho_1 d^3\rho_2\ldots d^3\rho_i d^3\rho_2'\ldots d^3\rho_j' L^{(ij)} \times(\mathbf{r}_1;\mathbf{r}_2\ldots\mathbf{r}_i;\mathbf{r}_2'\ldots\mathbf{r}_j')\nabla_1\delta u_i^*(\mathbf{r}_1,\mathbf{r}_2\ldots\mathbf{r}_i;t) \cdot\nabla_1\delta u_j(\mathbf{r}_1,\mathbf{r}_2'\ldots\mathbf{r}_j';t). \quad (3.8)$$

The coefficient functions $L^{(ij)}(\mathbf{r}_1;\mathbf{r}_2\ldots\mathbf{r}_i;\mathbf{r}_2'\ldots\mathbf{r}_j')$ are expressed in terms of ground-state distribution functions, as spelled out in Appendix A3. Next, we collect all terms that contain $\delta u_1(\mathbf{r};t)$ into the current (2.12). With the abbreviation

$$\mathbf{v}(\mathbf{r};t) \equiv \frac{\mathbf{j}(\mathbf{r};t)}{\rho_1(\mathbf{r})} \quad (3.9)$$

for the velocity field, the interaction Lagrangian becomes

$$\mathcal{L}_{\rm int}(t) = \frac{m}{2}\int d^3\rho|\mathbf{v}(\mathbf{r};t)|^2 + \sum_{i,j=2}^{3}\mathcal{L}_{\rm int}^{\prime(ij)}(t), \quad (3.10)$$

where the individual terms have again the structure (3.8) but with different coefficient functions $L^{\prime(ij)}(\mathbf{r}_1;\mathbf{r}_2\ldots\mathbf{r}_i;\mathbf{r}_2'\ldots\mathbf{r}_j')$.

The last step is to eliminate the $\delta u_2(\mathbf{r}_i,\mathbf{r}_j;t)$ using Eq. (2.10). The general structure of the result is

$$\mathcal{L}_{\rm int}(t) = \frac{m}{2}\int d^3\rho|\mathbf{v}(\mathbf{r};t)|^2 + \sum_{i=2}^{3}\mathcal{L}_{\rm int}^{\prime\prime(ii)}(t), \quad (3.11)$$

where the $\mathcal{L}_{\rm int}^{\prime\prime(ii)}(t)$ are now functionals of $\delta v_2(\mathbf{r}_i,\mathbf{r}_j;t)$ and $\delta v_3(\mathbf{r}_i,\mathbf{r}_j,\mathbf{r}_k;t)$. We use Eq. (2.10) to simplify this expression and obtain the form

$$\mathcal{L}_{\rm int}^{\prime\prime(2,2)}(t) = \frac{\hbar^2}{8m}\int d^3\rho_1 d^3\rho_2 d^3\rho_2'\mathcal{F}_{22}(\mathbf{r}_1;\mathbf{r}_2,\mathbf{r}_2')\delta\mathbf{Q}(\mathbf{r}_1,\mathbf{r}_2;t) \cdot\delta\mathbf{Q}^*(\mathbf{r}_1,\mathbf{r}_2';t), \quad (3.12)$$

where $\mathcal{F}_{22}(\mathbf{r}_1;\mathbf{r}_2,\mathbf{r}_2')$ is given in Eq. (A11) [4] and

$$\delta\mathbf{Q}(\mathbf{r}_1,\mathbf{r}_2;t) \equiv \nabla_{\mathbf{r}_1}\delta v_2(\mathbf{r}_1,\mathbf{r}_2;t) - \int d^3\rho_1' d^3\rho_2' d^3\rho_3'\delta v_3(\mathbf{r}_1',\mathbf{r}_2',\mathbf{r}_3';t) \times\nabla_{\mathbf{r}_1}\mathcal{G}_{23}(\mathbf{r}_1,\mathbf{r}_2;\mathbf{r}_1',\mathbf{r}_2',\mathbf{r}_3'), \quad (3.13)$$

where $\mathcal{G}_{23}$ is defined in Eq. (2.11).

Finally,

$$\mathcal{L}_{\rm int}^{\prime\prime(3,3)}(t) = \frac{\hbar^2}{16m}\int d^3\rho_1\ldots d^3\rho_3'\mathcal{F}_{33}(\mathbf{r}_1;\mathbf{r}_2,\mathbf{r}_3;\mathbf{r}_2',\mathbf{r}_3')\nabla_{\mathbf{r}_1} \times\delta v_3(\mathbf{r}_1,\mathbf{r}_2,\mathbf{r}_3;t)\cdot\nabla_{\mathbf{r}_1}\delta v_3^*(\mathbf{r}_1,\mathbf{r}_2',\mathbf{r}_3';t) \quad (3.14)$$

and the function $\mathcal{F}_{33}(\mathbf{r}_1;\mathbf{r}_2,\mathbf{r}_3;\mathbf{r}_2',\mathbf{r}_3')$, defined in Eq. (A16), is a combination of ground-state distribution functions that will have to be dealt with in a diagrammatic analysis.

IV. EQUATIONS OF MOTION

A. General structure

We make the standard decomposition

$$\begin{aligned}\delta V_{\rm ext}(\mathbf{r};t) &= \delta V_{\rm ext}(\mathbf{r})[e^{i\omega t}+e^{-i\omega t}],\\ \delta v_n(\mathbf{r}_1,\ldots,\mathbf{r}_n;t) &= v_n^{(+)}(\mathbf{r}_1,\ldots,\mathbf{r}_n)e^{-i\omega t}\\ &\quad + v_n^{(-)}(\mathbf{r}_1,\ldots,\mathbf{r}_n)e^{i\omega t},\\ \delta\rho_1(\mathbf{r};t) &= \delta\rho_1^{(+)}(\mathbf{r})e^{-i\omega t}+\delta\rho_1^{(-)}(\mathbf{r})e^{i\omega t}.\\ \mathbf{j}(\mathbf{r};t) &= \mathbf{j}^{(+)}(\mathbf{r})e^{-i\omega t}+\mathbf{j}^{(-)}(\mathbf{r})e^{i\omega t}\end{aligned} \quad (4.1)$$

We can do the harmonic decomposition of all time-dependent functions at this point whereby the $i\hbar\partial/\partial t$ is replaced by $\hbar\omega$ when acting on $e^{-i\omega t}$, etc. In particular, one can think of all pair and triplet fluctuations as functions of only one frequency because the pair equations with positive and negative frequency decouple. Only the one-body equation will eventually give us a superposition of positive and negative frequencies.

The next steps in our derivations are largely independent of the actual approximations used for calculating the combinations of distribution functions entering the Lagrangian; in fact, we will see that we can reduce the equations of motion to a form that is almost identical to that of the pair fluctuation version of the theory [4]. The one-body equation is simply the continuity equation

$$\nabla\cdot\mathbf{j}(\mathbf{r};t)+\dot\rho(\mathbf{r};t) = \frac{2}{i\hbar}\rho_1(\mathbf{r})\int d^3\rho' S(\mathbf{r},\mathbf{r}')\delta V_{\rm ext}(\mathbf{r}';t), \quad (4.2)$$

where the current is given by Eq. (2.17), $S(\mathbf{r},\mathbf{r}')$ is defined in Eq. (2.6), and the relationship between $\dot\rho(\mathbf{r};t)$ and $\delta\dot v_1(\mathbf{r};t)$ is given by the time derivative of Eq. (2.5). The equations for the pair and triplet fluctuations are derived by variation of the Lagrangian; in particular, the general form of the three-body equation is quite complicated and calls for simplifications which we will outline in the next section and carry out in detail in Appendix B. It is important to note that the one-body current does not contain three-body fluctuations. This means we can express the three-body fluctuations in terms of pair fluctuations alone.

B. Convolution approximation

It still takes a number of manipulations to derive a set of equations of motion in a form that is both structurally plausible and numerically practical. HNC equations for all the basic ingredients of the theory were solved in Ref. [4]. This required, among others, the calculation of the three-point function $\mathcal{F}_{22}(\mathbf{r}_1;\mathbf{r}_2,\mathbf{r}_2')$ and the four-point function $\delta g_2(\mathbf{r}_1,\mathbf{r}_2)/\delta u_2(\mathbf{r}_1',\mathbf{r}_2')$. That calculation was feasible in a partial wave expansion; however, trying to do the same at the three-body level would imply dealing with six-point functions. Before entering such a tedious calculation, the inclusion of three-body fluctuations should be attempted at a much simpler level. Therefore, the first objective is to include triplet fluctuations in the convolution approximation [43,57,58]. We use the convolution approximation as the simplest approximation that ensures that the long-wavelength behavior is correct. This

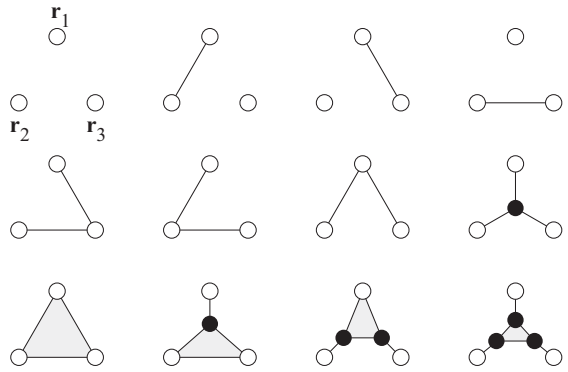

FIG. 2. Diagrammatic representation of the three-body distribution function. The upper two lines constitute the convolution approximation. The solid line represents a function $h(\mathbf{r}_i,\mathbf{r}_j)$ defined in Eq. (4.4) and the shaded triangle in the third line represents the nonnodal three-body function $X_3(\mathbf{r}_1,\mathbf{r}_2,\mathbf{r}_3)$. In leading order, this function is approximated by the triplet correlation function $u_3(\mathbf{r}_1,\mathbf{r}_2,\mathbf{r}_3)$. Not all diagrams that can be generated by symmetry operations are shown.

is also the simplest approximation that satisfies the sequential relations between the n-body densities.

The reassuring result of Ref. [4] was that the convolution approximation is, in fact, quite good when used in conjunction with the "unrenormalized" form of the self-energy. We shall see that the implementation of our present theory is, at this level, also quite feasible and permits, unlike the full theory, an intuitive physical interpretation.

In order to calculate the ingredients of the diagonalized interaction Lagrangian [Eqs. (3.11)–(3.14)], we need to evaluate the two-point vector fluctuation function $\delta\mathbf{Q}(\mathbf{r}_1,\mathbf{r}_2;t)$ [Eq. (3.13)] and two static functions depending only on ground-state distributions: $\mathcal{F}_{33}(\mathbf{r}_1;\mathbf{r}_2,\mathbf{r}_3;\mathbf{r}'_2,\mathbf{r}'_3)$, defined in Eq. (A16), and $\mathcal{G}_{23}(\mathbf{r}_1,\mathbf{r}_2;\mathbf{r}'_1,\mathbf{r}'_2,\mathbf{r}'_3)$, defined in Eq. (2.11). In addition, for the triplet variation of the time-dependent term in the Lagrangian [Eq. (A8)], we need the six-point static function $\delta g_3(\mathbf{r}_1,\mathbf{r}_2,\mathbf{r}_3)/\delta u_3(\mathbf{r}'_1,\mathbf{r}'_2,\mathbf{r}'_3)$.

Let us first look at the second term in Eq. (3.13). The diagrammatic expansion of the three-body distribution function is shown in Fig. 2; the convolution approximation constitutes the set of diagrams shown in the first two rows. The graphical representation of the function $\mathcal{G}_{23}(\mathbf{r}_1,\mathbf{r}_2;\mathbf{r}'_1,\mathbf{r}'_2,\mathbf{r}'_3)$ is obtained by removing, in turn, a line from the graphical representation of the three-body function. If the line is connected to one of the external points $\mathbf{r}'_i$, $i=1\ldots3$, a $\delta(\mathbf{r}'_i-\mathbf{r}_j)/\rho(\mathbf{r}_j)$ is added. The representation of the first few diagrams contributing to $\mathcal{G}_{23}(\mathbf{r}_1,\mathbf{r}_2;\mathbf{r}'_1,\mathbf{r}'_2,\mathbf{r}'_3)$ is shown in Fig. 3.

Adopting the convolution approximation for $g_3(\mathbf{r}'_1,\mathbf{r}'_2,\mathbf{r}'_3)$, it is straightforward to calculate the second term in Eq. (3.13) for $\delta\mathbf{Q}$:

$$\begin{aligned}&\int d^3\rho'_1 d^3\rho'_2 d^3\rho'_3\,\delta v_3(\mathbf{r}'_1,\mathbf{r}'_2,\mathbf{r}'_3;t)\nabla_{\mathbf{r}_1}\mathcal{G}_{23}(\mathbf{r}_1,\mathbf{r}_2;\mathbf{r}'_1,\mathbf{r}'_2,\mathbf{r}'_3)\\ &\quad\approx\int d^3\rho'_3\nabla_1 h(\mathbf{r}_1,\mathbf{r}'_3)\delta v_3(\mathbf{r}_1,\mathbf{r}_2,\mathbf{r}'_3)\\ &\qquad+\frac{1}{2}\int d^3\rho'_3 d^3\rho'_4\nabla_1[h(\mathbf{r}_1,\mathbf{r}'_3)h(\mathbf{r}_1,\mathbf{r}'_4)]\delta v_3(\mathbf{r}_2,\mathbf{r}'_3,\mathbf{r}'_4),\end{aligned}\tag{4.3}$$

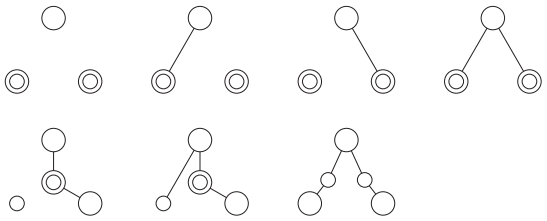

FIG. 3. Diagrammatic representation of the function $\mathcal{G}_{23}(\mathbf{r}_1,\mathbf{r}_2;\mathbf{r}'_1,\mathbf{r}'_2,\mathbf{r}'_3)$. Small circles correspond to the points $\mathbf{r}_j$, $j=1,2$, and large circles to the points $\mathbf{r}'_i$, $i=1\ldots3$. If a small circle and a large circle coincide, it is understood that a function $\delta(\mathbf{r}_i-\mathbf{r}'_j)/\rho(\mathbf{r}'_j)$ is added. The entire expression must be symmetrized with respect to the points $\mathbf{r}_j$, $j=1,2$, and $\mathbf{r}'_i$, $i=1\ldots3$. The first three diagrams shown in the upper row and the first diagram in the lower row constitute the convolution approximation.

where

$$h(\mathbf{r},\mathbf{r}')\equiv g_2(\mathbf{r},\mathbf{r}')-1.\tag{4.4}$$

We see here the beginning of the series of diagrams representing the function $\mathbf{W}_2(\mathbf{r}_1;\mathbf{r}'_1,\mathbf{r}'_2)$ [Eq. (2.14)]. Higher-order diagrams contributing to $\mathbf{W}_2(\mathbf{r}_1;\mathbf{r}'_1,\mathbf{r}'_2)$ are generated by the subset of contributions to $g_3(\mathbf{r}_1,\mathbf{r}_2,\mathbf{r}_3)$ that have a node between one of the external points and the other two. Thus, we can write

$$\begin{aligned}\delta\mathbf{Q}^{(\mathrm{CA})}(\mathbf{r}_1,\mathbf{r}_2)&=\nabla_{\mathbf{r}_1}\delta v_2(\mathbf{r}_1,\mathbf{r}_2)\\ &\quad-\frac{1}{2}\int d^3\rho'_3 d^3\rho'_4\mathbf{W}_2(\mathbf{r}_1;\mathbf{r}'_3,\mathbf{r}'_4)\delta v_3(\mathbf{r}_2,\mathbf{r}'_3,\mathbf{r}'_4).\end{aligned}\tag{4.5}$$

The calculation of the variation $\delta g_3(\mathbf{r}'_1,\mathbf{r}'_2,\mathbf{r}'_3)/\delta u_3(\mathbf{r}_1,\mathbf{r}_2,\mathbf{r}_3)$ is the most tedious one because this function contains up to six-body distribution functions. The "convolution approximation" amounts to keeping all diagrams with a fixed difference between the number of points and the number of lines. Specifically, in the six-body distribution function contributing to $\delta g_3(\mathbf{r}'_1,\mathbf{r}'_2,\mathbf{r}'_3)/\delta u_3(\mathbf{r}_1,\mathbf{r}_2,\mathbf{r}_3)$ we keep all diagrams with three lines $h(\mathbf{r}_i,\mathbf{r}_j)$, in the five-body term all contributions with two lines, etc. This amounts to the approximation

$$\begin{aligned}\left[\frac{\delta g_3(\mathbf{r}'_1,\mathbf{r}'_2,\mathbf{r}'_3)}{\delta u_3(\mathbf{r}_1,\mathbf{r}_2,\mathbf{r}_3)}\right]^{(CA)}&=\rho_1(\mathbf{r}'_1)\rho_1(\mathbf{r}'_2)\rho_1(\mathbf{r}'_3)\\ &\quad\times[S(\mathbf{r}_1,\mathbf{r}'_1)S(\mathbf{r}_2,\mathbf{r}'_2)S(\mathbf{r}_3,\mathbf{r}'_3)+\mathrm{cycl.}].\end{aligned}\tag{4.6}$$

The calculation of $\mathcal{F}_{33}(\mathbf{r}_1;\mathbf{r}_2,\mathbf{r}_3;\mathbf{r}'_2,\mathbf{r}'_3)$ is somewhat more tedious due to the subtraction term spelled out in the last line of Eq. (A16). To get all five-point diagrams with two lines, one must also keep all two-line diagrams in $\mathcal{F}_{33}(\mathbf{r}_1;\mathbf{r}_2,\mathbf{r}_2;\mathbf{r}'_2,\mathbf{r}_3)$. Nevertheless, the result is simple and as expected:

$$\mathcal{F}_{33}^{(CA)}(\mathbf{r}_1;\mathbf{r}_2,\mathbf{r}_3;\mathbf{r}'_2,\mathbf{r}'_3)=S(\mathbf{r}_2,\mathbf{r}'_2)S(\mathbf{r}_3,\mathbf{r}'_3)+S(\mathbf{r}_2,\mathbf{r}'_3)S(\mathbf{r}_3,\mathbf{r}'_2)\tag{4.7}$$

The remaining, somewhat complicated, calculations can be found in Appendix B for the general case of an inhomogeneous system. We proceed here to spell out the case of a translationally invariant geometry.

The Feynman states, defined in general in Eq. (B2), are plane waves in the uniform system:

$$\psi_n(\mathbf{r}) = \sqrt{\frac{1}{\Omega S(k_n)}} e^{i\mathbf{k}_n\cdot\mathbf{r}} \quad \phi_n(\mathbf{r}) = \sqrt{\frac{S(k_n)}{\Omega}} e^{i\mathbf{k}_m\cdot\mathbf{r}}, \tag{4.8}$$

where Ω is the normalization volume. The self-energy matrix becomes diagonal, and the density-density response function is

$$\chi(k,\hbar\omega) = \frac{S(k)}{\hbar\omega - \Sigma(k,\hbar\omega)} + \frac{S(k)}{-\hbar\omega - \Sigma(k,-\hbar\omega)}, \tag{4.9}$$

where

$$\begin{aligned}\Sigma(k,\hbar\omega) &= \varepsilon_0(k) + \frac{1}{2}\int \frac{d^3p\, d^3q}{(2\pi)^3\rho}\delta(\mathbf{k}-\mathbf{p}-\mathbf{q}) \\ &\times \frac{|V_3(\mathbf{k};\mathbf{p},\mathbf{q})|^2}{\hbar\omega - \Sigma[p,\hbar\omega-\varepsilon_0(q)] - \Sigma[q,\hbar\omega-\varepsilon_0(p)]}.\end{aligned} \tag{4.10}$$

V_3 is proportional to the two-phonon hybridization vertex, given in terms of ground-state quantities as [46]

$$\begin{aligned}\frac{V_3(\mathbf{k};\mathbf{p},\mathbf{q})}{\sqrt{N}} &\equiv \langle\Psi^{(0)}_{\mathbf{k},\mathbf{q}}|\delta H|\Psi^{(0)}_{\mathbf{k}}\rangle \\ &= \frac{\hbar^2}{2m}\sqrt{\frac{S(p)S(q)}{NS(k)}}[\mathbf{k}\cdot\mathbf{p}\tilde{X}(p) + \mathbf{k}\cdot\mathbf{q}\tilde{X}(q) \\ &- k^2\tilde{u}_3(\mathbf{k},\mathbf{p},\mathbf{q})],\end{aligned} \tag{4.11}$$

where

$$\tilde{X}(k) = 1 - \frac{1}{S(k)} \tag{4.12}$$

is the direct correlation function, and $\tilde{u}_3(\mathbf{k},\mathbf{p},\mathbf{q})$ is the dimensionless Fourier transform of the static three-body correlation function u_3 of Eq. (1.18). If the self-energy is real, the pole strength of $\chi(k,\hbar\omega)$ determines the strength $Z(k)$ of the single-phonon excitation, whereas the imaginary part of $\Sigma(p,\hbar\omega)$ characterizes the multiexcitation continuum.

Note that Eq. (4.10) defines an iterative procedure, we have above proven only the first step. The diagrammatic analysis in terms of BW perturbation theory in the next section gives justification for our procedure.

V. BRILLOUIN-WIGNER PERTURBATION THEORY: AN ALTERNATIVE APPROACH

An alternative method to study the excitations of interest here is Brillouin-Wigner (BW) perturbation theory in a suitably chosen correlated basis [20,43–46,61]. As applied in these references, BW perturbation theory provides the energy of the lowest-lying excitations, whereas the equations-of-motion method generates the full density-density response function whose features may be interpreted in terms of single-excitation and multiexcitation energies of eigenstates which couple to the correlated density fluctuations [see Eq. (1.2)]. It should be clear that, to the extent that the same physics is described, BW perturbation theory and the present EOM approach should lead to the same results. Specifically, the EOM method gives the full response function and, *consequently*, also the lowest-excitation mode. BW gives only the lowest excitation. On the other hand, it is relatively simple to extend BW perturbation theory to higher order [20], whereas the equations-of-motion method is even at third order rather cumbersome. The equations-of-motion method leads, at the level elaborated here, to an expression for the self-energy (4.10) that contains the second-order approximation [45,46] in the energy denominator. The analogy with BW perturbation theory provides the justification for considering Eq. (4.10) as a self-consistency problem.

In our application of BW perturbation theory, the basis states comprise correlated basis functions generated by repeated application of the density fluctuation operator to the ground state, e.g.,

$$\begin{aligned}|\Psi^{(0)}_{\mathbf{k}}\rangle &= \frac{1}{\sqrt{NS(k)}}\rho_{\mathbf{k}}|\Psi_0\rangle, \\ |\Psi^{(0)}_{\mathbf{k},\mathbf{q}}\rangle &= \frac{1}{\sqrt{N^2S(k)S(q)}}\rho_{\mathbf{k}}\rho_{\mathbf{q}}|\Psi_0\rangle.\end{aligned} \tag{5.1}$$

The first of these states is the single Feynman phonon state, defined below Eq. (1.4), with corresponding Bijl-Feynman excitation energy $\varepsilon_0(k) \equiv \hbar^2k^2/2mS(k)$. The second state in Eq. (5.1) is the primary component of the two-Feynman-phonon state that has an energy $\varepsilon_0(k) + \varepsilon_0(q)$. The obvious

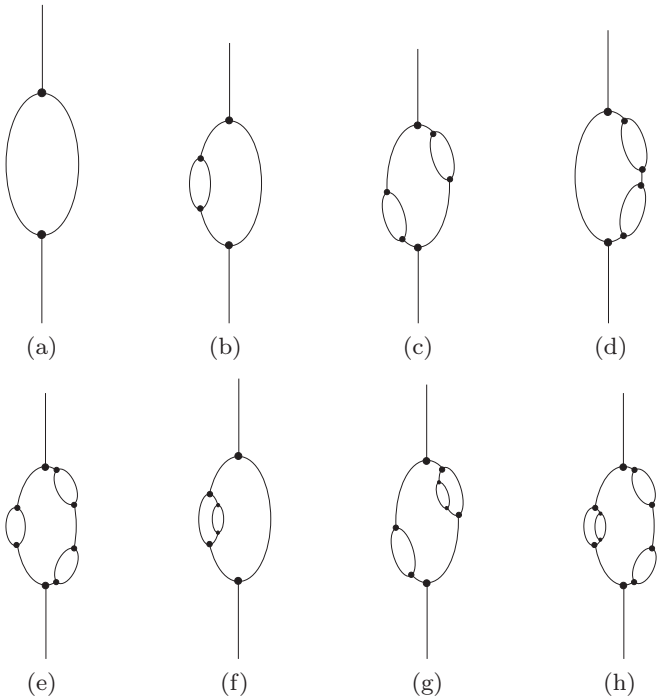

FIG. 4. Beginning of the series of Feynman diagrams representing the self-energy $\Sigma^{(1)}(k,\hbar\omega)$ at the triplet level of the EOM. Diagram (a) corresponds to the self-energy correction to $\varepsilon_0(k)$ in $\Sigma^{(0)}(k,\hbar\omega)$ at the pair level, where an incoming phonon splits into two that recombine again. Diagrams (b)–(e) indicate the beginning of the series which renormalizes diagram (a) to $\Sigma^{(1)}(k,\hbar\omega)$. Dressing the sub-bubbles of the so-generated diagrams with diagram (a), examples of which are shown in diagrams (f)–(h), and chains of it leads to $\Sigma^{(2)}(k,\hbar\omega)$, and so on. Topologically equivalent diagrams are omitted.

generalization of these states to the set of M^{th}-order multinomials in the density fluctuation factors, with $M \leqslant N$, correlated by $|\Psi_0\rangle$, forms a complete, correlated basis [23].

The unperturbed state for the elementary excitation of interest is the Feynman state $|\Psi_{\mathbf{k}}^{(0)}\rangle$. The corresponding perturbing Hamiltonian is

$$\delta H \equiv H - \langle\Psi_{\mathbf{k}}^{(0)}|H|\Psi_{\mathbf{k}}^{(0)}\rangle = H - E_0 - \varepsilon_0(k), \tag{5.2}$$

where the subtraction of $\varepsilon_0(k)$ accounts for the nonorthogonality of the one-phonon (Feynman) state to the two-phonon states in Eq. (5.1). The zeroth-order excitation energy is just the Feynman energy $\varepsilon_0(k)$; the first-order contribution vanishes. In second order, one finds the well-known relationship

$$\begin{aligned}\varepsilon(k) &= \Sigma^{(0)}[k,\varepsilon(k)] \\ &= \varepsilon_0(k) + \frac{1}{2}\int \frac{d^3p\,d^3q}{(2\pi)^3\rho}\delta(\mathbf{k}-\mathbf{q}-\mathbf{p}) \\ &\quad\times \frac{|V_3(\mathbf{k};\mathbf{p},\mathbf{q})|^2}{\varepsilon(k)-\varepsilon_0(p)-\varepsilon_0(q)},\end{aligned} \tag{5.3}$$

where V_3 is defined in Eq. (4.11). We have used here the notation used in previous work [20,43–46,61]. It is understood that Eq. (5.3) is to be solved self-consistently for $\varepsilon(k)$.

The second-order expression for the excitation energy is represented in terms of Feynman diagrams by Fig. 4(a). This is equivalent to the excitation energy obtained from the unrenormalized self-energy $\Sigma^{(0)}(k,\hbar\omega)$ at the level of pair fluctuations in the convolution approximation.

In order to make connection to the result of the EOM at the triplet level described here, one has to sum diagrams containing three phonon vertices of the type in Eq. (4.11). Examples are shown in Fig. 4. Due to the appearance of $\Sigma^{(0)}(k,\hbar\omega)$ in the calculation of the self-energy $\Sigma^{(1)}(k,\hbar\omega)$ at the triplet level, we find that the corresponding *infinite* class of Feynman diagrams can be obtained by replacing the intermediate phonons in Fig. 4(a) with the diagram itself and chains of it, respectively. The beginning of this series is given by diagrams in Figs. 4(b)–4(h) and can be summed easily. The energy contribution of Fig. 4(a) is called $\epsilon_{\text{a}}(k,\hbar\omega)$, that of Fig. 4(b) $\epsilon_{\text{b}}(k,\hbar\omega)$, and so on. One finds

$$\begin{aligned}\Sigma^{(1)}(k,\hbar\omega) &= \varepsilon_0(k) + \epsilon_{\text{a}}(k,\hbar\omega) + \epsilon_{\text{b}}(k,\hbar\omega) + \cdots \\ &\equiv \varepsilon_0(k) + \epsilon_{\text{a}}^{(1)}(k,\hbar\omega) \\ &= \varepsilon_0(k) + \frac{1}{2}\int \frac{d^3p\,d^3q}{(2\pi)^3\rho}\delta(\mathbf{p}+\mathbf{q}+\mathbf{k})\frac{|V_3(\mathbf{k};\mathbf{p},\mathbf{q})|^2}{\hbar\omega-\varepsilon_0(p)-\varepsilon_0(q)}\sum_{M=0}\sum_{n=0}\binom{M}{n}\frac{\epsilon_{\text{a}}^{M-n}[p,\hbar\omega-\varepsilon_0(q)]\epsilon_{\text{a}}^{n}[q,\hbar\omega-\varepsilon_0(p)]}{[\hbar\omega-\varepsilon_0(p)-\varepsilon_0(q)]^M} \\ &= \varepsilon_0(k) + \frac{1}{2}\int \frac{d^3p\,d^3q}{(2\pi)^3\rho}\delta(\mathbf{p}+\mathbf{q}+\mathbf{k})\frac{|V_3(\mathbf{k};\mathbf{p},\mathbf{q})|^2}{\hbar\omega-\varepsilon_0(p)-\varepsilon_0(q)}\sum_{M=0}\left(\frac{\epsilon_{\text{a}}[p,\hbar\omega-\varepsilon_0(q)]+\epsilon_{\text{a}}[q,\hbar\omega-\varepsilon_0(p)]}{\hbar\omega-\varepsilon_0(p)-\varepsilon_0(q)}\right)^M \\ &= \varepsilon_0(k) + \frac{1}{2}\int \frac{d^3p\,d^3q}{(2\pi)^3\rho}\delta(\mathbf{p}+\mathbf{q}+\mathbf{k})\frac{|V_3(\mathbf{k};\mathbf{p},\mathbf{q})|^2}{\hbar\omega-\varepsilon_0(p)-\varepsilon_0(q)-\epsilon_{\text{a}}[p,\hbar\omega-\varepsilon_0(q)]-\epsilon_{\text{a}}[q,\hbar\omega-\varepsilon_0(p)]} \\ &= \varepsilon_0(k) + \frac{1}{2}\int \frac{d^3p\,d^3q}{(2\pi)^3\rho}\delta(\mathbf{p}+\mathbf{q}+\mathbf{k})\frac{|V_3(\mathbf{k};\mathbf{p},\mathbf{q})|^2}{\hbar\omega-\Sigma^{(0)}[p,\hbar\omega-\varepsilon_0(q)]-\Sigma^{(0)}[q,\hbar\omega-\varepsilon_0(p)]},\end{aligned} \tag{5.4}$$

which is exactly our result from the EOM method at the triplet level.

Due to the intuitive formulation of perturbation theory in terms of Feynman diagrams, one can now easily prove the generalization of Eq. (5.4) to an implicit relation for the self-energy. Instead of dressing the first diagram in Fig. 4 with itself, one can dress it with a sum of diagrams, e.g., $\epsilon_{\text{a}}^{(1)}(k,\hbar\omega)$. Restricting the set of diagrams to those where no two dressed sub-bubbles exist at the same time, this procedure does not alter the form of Eq. (5.4), i.e., the weight factors stay the same so that the sum can be carried out to give

$$\Sigma^{(i)} = \Sigma^{(i)}[\Sigma^{(i-1)}] \tag{5.5}$$

with the same form as the EOM result for $i = 1$. Taking the limit $i \to \infty$ leads to Eq. (4.10) for the self-energy.

VI. RESULTS AND DISCUSSION

As mentioned above, we use the "unrenormalized" version of our theory together with the convolution approximation in our calculation of the dynamic structure function. From our previous work [4], we have determined that this approximation is an acceptable compromise between predictive power and numerical effort. In particular, we shall see that includes all those features in a quantitative manner that can be clearly identified in experiments. There are undeniable effects coming from multiphonon excitations. These are, however, mostly structureless and do not lend themselves to a clear identification of individual physical processes.

The input of all of our calculations are ground-state quantities for ^{4}He interacting via the phenomenological Aziz II potential [62]. With one adjustable parameter to correct for the poor convergence of the series of "elementary diagrams," the HNC-EL theory reproduces the experimental equation of state at the percent level [42,53]. More details on how we have dealt with ground-state triplet correlations may be found in Ref. [51].

To compare with experiments and with quantum Monte Carlo simulation data, we rely heavily on a recent study [5] which compares several quantities that are either experimentally accessible, can be calculated by simulations, or both. To demonstrate the quality of our ground-state calculation, we begin with a comparison of the pressure-density relationship. Such a comparison is important because the

FIG. 5. The figure shows the first diagram that is not included in the convolution approximation.

experimentally adjustable parameter is usually the pressure, whereas theoretical calculations are carried out at fixed density. Figure 6 shows the pressure-density relationship obtained from experiments [63,64], simulations [65], and our HNC-EL calculations [51]. Caupin *et al.* [5] find a very good fit to the equation of state using a cubic function suggested by Maris [66] for the pressure-density relationship of the form

$$p = p_s + \frac{b^2}{27}(\rho - \rho_s)^3, \tag{6.1}$$

where p_s and ρ_s are the pressure and the density at the spinodal point. Although the analytic form of the relationship (6.1) is incorrect in the vicinity of the spinodal point [51], it gives a good representation [5] of the experimental data [63,64] and diffusion Monte Carlo (DMC) simulations [65] in the experimentally accessible regime, as seen in Fig. 6. The FJEL results can be brought to a match with the other data by a slight horizontal displacement $\delta\rho = 0.0003$ Å^{-3} (approximately 1%); we demonstrate this by shifting the pressure-density relationship from our FJEL calculation horizontally by that amount in Fig. 6.

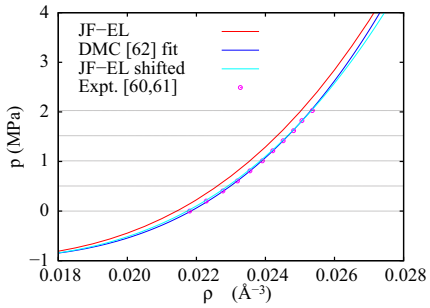

FIG. 6. (Color online) The figure shows several calculations and experiments of the pressure-density relationship of ^{4}He: our FJEL calculations (red upper curve); the fit (6.1) to the pressure derived from the DMC simulation equation of state of Ref. [65] (dark blue curve); the experimental pressure-density results of Refs. [63,64] (circles); and the FJEL relationship shifted by a density offset $\delta\rho = 0.0003$ Å^{-3} (light blue curve). The dotted horizontal lines at $p = 0, 0.5, 1.0, 1.5$, and 2.0 MPa are drawn into the figure to depict the densities where experimental data for the dynamic structure function are available.

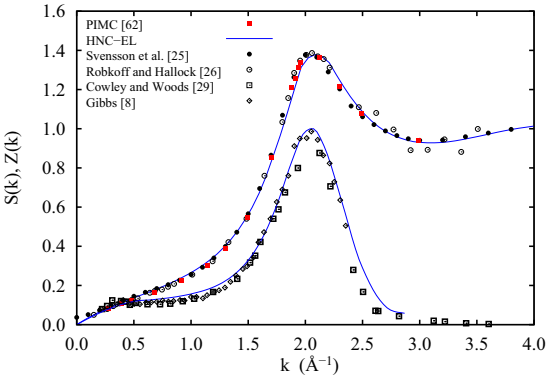

FIG. 7. (Color online) The figure shows calculations and experiments of the static structure function of ^{4}He at SVP: our FJEL calculations (blue upper curve); the experiments of Svensson *et al.* (Ref. [25], filled dots) and of Robkoff and Hallock (Ref. [26], circles); and simulation data (Ref. [65], red squares). We also show the strength of the single-phonon excitation (1.8) from our FJEL calculations (blue lower line), and from the experiments of Cowley and Woods [29] (boxes) and of Gibbs *et al.* [8] (squares).

The static structure function $S(k)$ is the most important ground-state quantity for the purpose of calculating the dynamics of the system; therefore, it is important that our ground-state theory provides reliable information. Figures 7 and 8 provide a comparison of our results with experimental and simulation results close to SVP, and at 2.0 MPa, corresponding to densities of $\rho = 0.022$ and 0.025 Å^{-3}, respectively. Our results at SVP are compared with the experimental data of Refs. [25,26] as well as the simulation data reviewed in Ref. [65]. In these two figures we also show a comparison of our results for the strength of the single-phonon excitation $Z(k)$ (1.8) from our FJEL calculations and experiments; we shall return to these results in our discussion of the dynamics.

The simulation data of Vranješ *et al.* [67] for $S(k)$ in Fig. 8, although at a slightly higher density than our FJEL calculation,

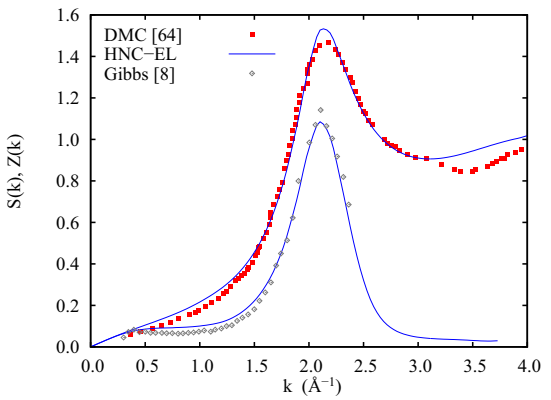

FIG. 8. (Color online) The figure shows FJEL calculations of the static structure function $S(k)$ of ^{4}He at a pressure of 2 MPa (upper blue curve) and the simulation data of Vranješ *et al.* [67] at a slightly higher density. We also show the strength of the single-phonon excitation (1.8) from our FJEL calculations (blue lower line) compared with the results of Gibbs *et al.* [8] (squares) at 2 MPa pressure.

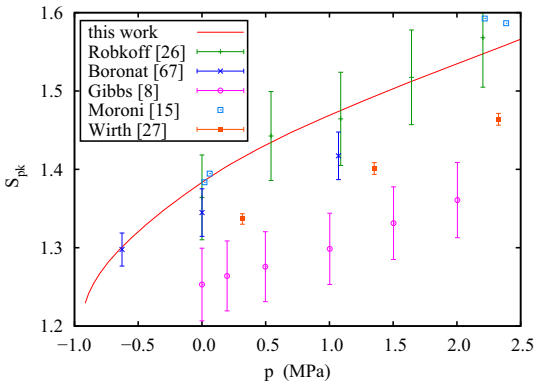

FIG. 9. (Color online) The figure shows a comparison of some of the experimental data [8,26,27,69], simulations [15,70], and our FJEL calculations for the peak of $S(k)$ as indicated in the inset.

predict a peak that is less than that predicted by the FJEL theory; the effect is even more visible when one compares with FJEL data at the same density. We have recently observed the same effect in ^{3}He in two dimensions [68], and will find a similar feature in the peak of the static response function below. The peak in $S(k)$ is related to long-ranged oscillations in the pair distribution function $g(r)$, caused by the impending liquid-solid phase transition. [We remind the reader that, in an isotropic, homogeneous fluid, the dimensionless pair density is the pair distribution function: $g_2(\mathbf{r}_1,\mathbf{r}_2) = g(r_{12})$; and $S(k) - 1$ is the dimensionless Fourier transform of $g(r) - 1$.] To get this peak right, one must have the pair distribution function at rather large distances; our FJEL calculations were carried out in a box of 200 Å. Replacing $g(r)$ for $r > 10$ Å with its asymptotic value of 1 and calculating the Fourier transform, this peak is much lowered. We are at this time not prepared to

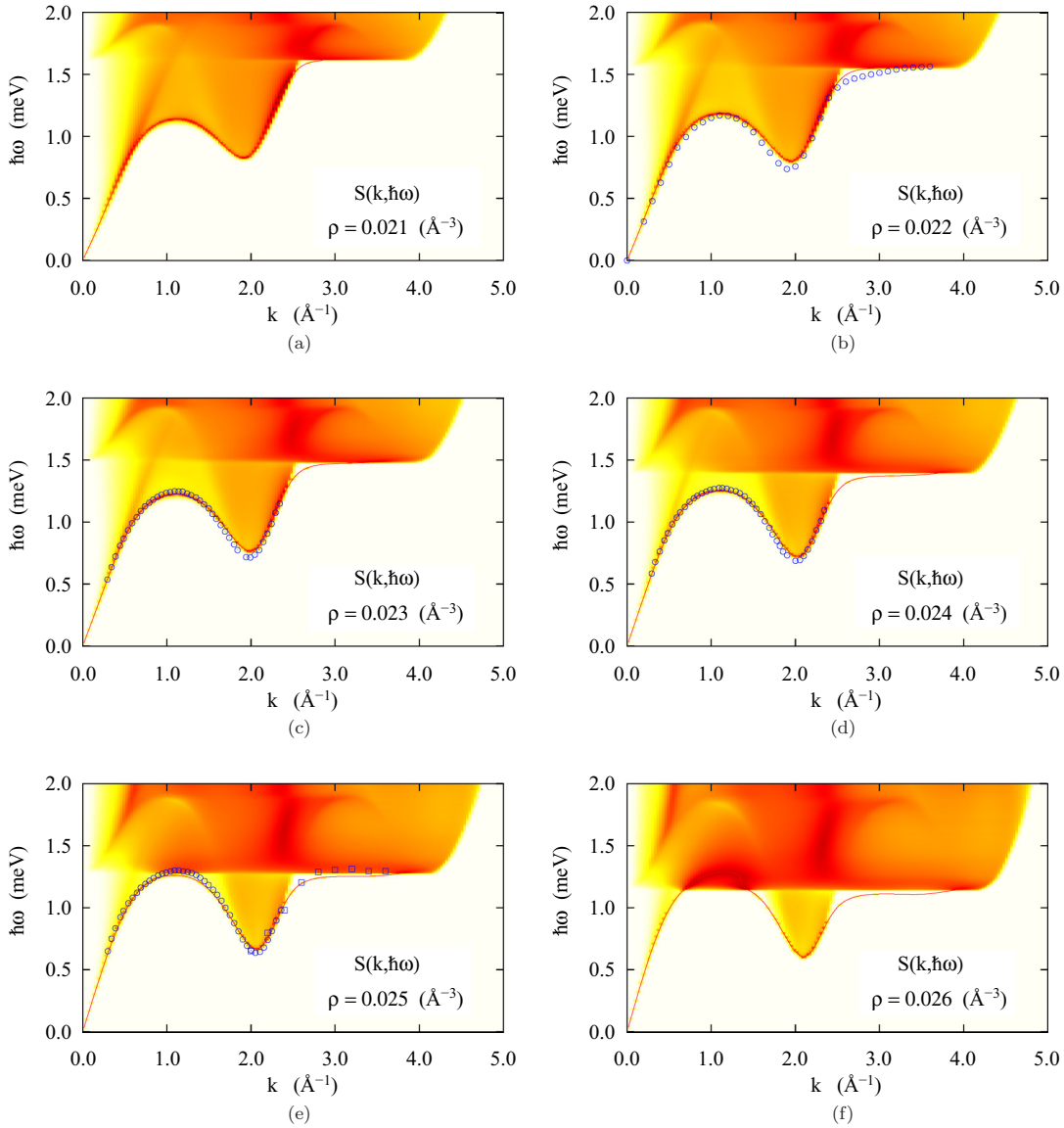

FIG. 10. (Color online) The figure shows color-coded (grayscale) plots of the dynamic structure function $S(k,\hbar\omega)$ for six different densities. Using a logarithmic scale, areas of high value of $S(k,\hbar\omega)$ are dark (orange to red), areas of low strength are light (yellow to white). Circles are experimental data for the phonon-roton dispersion relation from Ref. [29] in (b) and Ref. [8] at the higher densities where available. Squares in (e) are data from Ref. [7]. The red line is the solution of the dispersion relation (6.2) where it can be determined in a meaningful way.

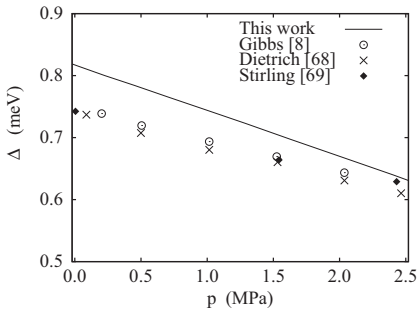

FIG. 11. The figure shows the roton energy Δ as a function of pressure obtained from our calculations (solid line) and a compilation of experimental data from Gibbs *et al.* [8] (circles), Dietrich *et al.* [71] (crosses), and Stirling [72] (diamonds).

attribute significance to this observation but the issue should be kept in mind.

A systematic account of the density/pressure dependence of the peak height of $S(k)$ is shown in Fig. 9. Most of the data have been taken from the compilation of earlier results provided in Ref. [5]; we have included our FJEL results with the simulation data and the selected experimental data as indicated in the figure. Evidently, our results fall well within the regime of different experiments and simulations.

Let us now turn to a discussion of our main results for the dynamics. A first account of our results can be seen from the maps of $S(k,\hbar\omega)$ shown in Figs. 10 for a sequence of densities. Also shown in the plots is the calculated phonon-roton dispersion relation (solid line) which is obtained by solving the nonlinear equation

$$\varepsilon(k) = \Sigma[k,\varepsilon(k)]\,. \tag{6.2}$$

We also show experimental data from Refs. [7,8,29] when available at that density.

A key quantity in the discussion of the excitations in ^{4}He is, of course, the "roton" [see Eq. (1.7)]. A compilation of experimental results and a comparison with the predictions of our calculations is shown in Figs. 11–13. As already seen from Fig. 10, the theoretical value of the roton energy is still a bit above the experimental value; this is to be expected from the correlated basis function BW calculations of Lee and Lee [20]. Their calculations did not use optimized correlation functions, nor ground-state correlations beyond $n = 2$. They should nevertheless give a reasonable estimate of the importance of higher-order diagrams, in particular the

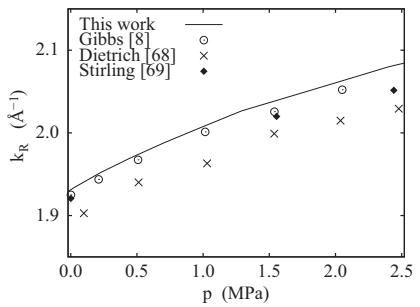

FIG. 12. Same as Fig. 11 for the roton momentum k_R.

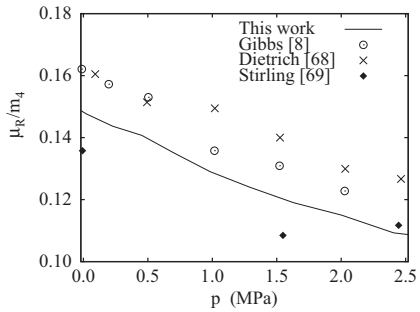

FIG. 13. Same as Fig. 11 for the roton "mass" μ_R in units of the ^{4}He mass.

diagram shown in Fig. 5. The first diagram that goes beyond the convolution approximation, shown in Fig. 5, is not contained in our calculation. According to Lee and Lee's estimates, the contribution of this diagram lowers the roton energy by about 0.05 meV. The apparent improvement of the agreement between theory and experiment with increasing density should be seen in the light of that estimate: We expect that the inclusion of such effects would shift the whole curve down by that amount, improving the agreement at lower densities and making it worse at higher densities.

The agreement between theory and experiment for both the roton wave number and the "mass" is quite satisfactory (see Figs. 12 and 13). Among those results, the roton "mass" has the largest uncertainty: All three quantities Δ_R, k_R, and μ_R are obtained by fitting the calculated spectrum in the vicinity of the roton minimum by the form (1.7). It turns out that μ_R is the most sensitive quantity of these three. Some smoothing of our results has, therefore, been done.

We have already above shown some results for the strength factor $Z(k)$ of the single-phonon excitation in Figs. 7 and 8. At different densities, the function $Z(k)$ looks similar; typically, the relative strength of the single-phonon excitation increases with pressure. Figure 14 shows our results and a comparison with some experimental and simulation data. It appears that our results are somewhat below the experimental values of Gibbs *et al.* [8] but above the simulation data of Ref. [73],

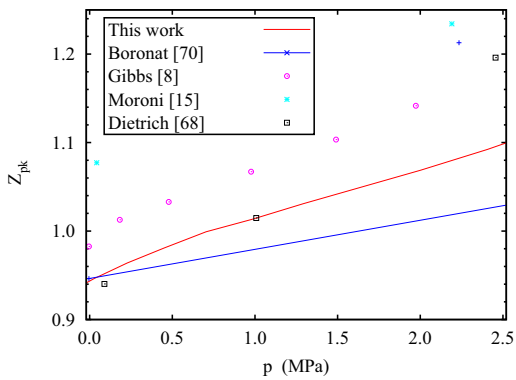

FIG. 14. (Color online) The figure shows a comparison of some of the experimental data [8,71] (circles and boxes), simulations of Boronat and Casulleras [73] (blue line), and Moroni *et al.* [15] (stars) with our FJEL calculations for the peak of $Z(k)$ as indicated in the inset.

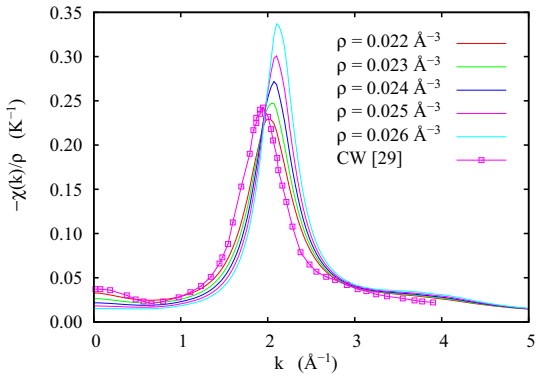

FIG. 15. (Color online) The figure shows a comparison of some of the experimental data with our EOM calculations of the static response function as a function of pressure and density as indicated in the inset. The simulation data of Ref. [74] are practically identical to the experimental data and not shown.

whereas the calculations of Moroni *et al.* [15] appear to predict a peak value of $Z(k)$ that is visibly higher. The issue definitely deserves further investigation.

Another simple quantity is the static response function $\chi(k,\hbar\omega = 0)$. This quantity can be obtained directly from our theory, setting $\omega = 0$ in Eq. (4.9); there is no need for using sum rules. Figure 15 shows a family of our results for $\chi(k)$ from our calculations; an extensive comparison of the peak height of $\chi(k,\hbar\omega = 0)$ is shown in Fig. 16.

Turning to the full $S(k,\hbar\omega)$ maps shown in Fig. 10 we see, of course, the well-known features: the phonon-roton spectrum turning eventually into the "Pitaevskii plateau." We display in these figures experimental data for the phonon-roton spectrum as far as available [7,8,29]. Looking only at these figures, we see that the agreement between experiments and theory is actually quite impressive. However, the $S(k,\hbar\omega)$ maps show more features: At long wavelengths, we see some strength along a line extrapolating from the phonon. Moreover, the "plateau" seems to have an extension towards longer wavelengths. Finally, we see some strength well above the maxon.

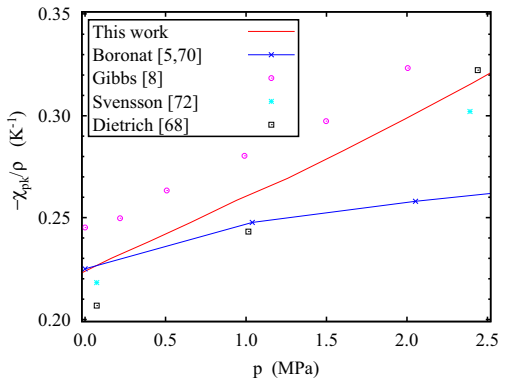

FIG. 16. (Color online) The figure shows a comparison of some of the experimental data [8,71,75] (circles, boxes, and stars), simulations of Boronat and Casulleras [5,73] (blue line) with our FJEL calculations for the peak of the static response function as a function of pressure as indicated in the inset.

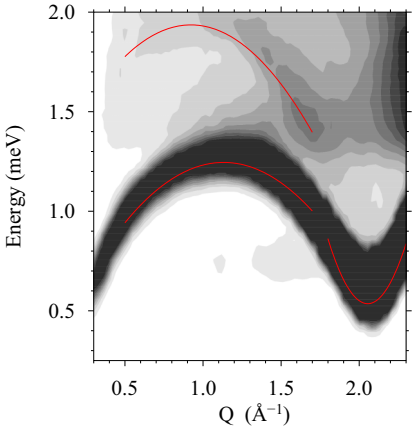

FIG. 17. (Color online) The figure shows the low-energy portion of the dynamic structure function at $p = 20$ Atm from Ref. [8]. The red lines in the figure are the roton data taken from Table 1 of [8], the maxon data fit to Fig. 10 of that paper, and the threshold energy (6.6). The grayscale data are reproduced from Ref. [8] with the permission of IOP Publishing and the authors.

Some of these features have also been seen weakly in experiments (see Fig. 17). More recent high-precision measurements of $S(k,\hbar\omega)$ show the above three effects much more clearly [76,77]; we discuss these features now in detail.

The physics behind the above-mentioned three features is the same; it originates from the possibility of the decay of an excitation into two sharp excitations. The issue is most transparently discussed if we assume that the energy denominator in Eq. (4.10) is reasonably well approximated by a collective mode, i.e., the self-energy has the form shown in Eq. (5.3), with the Feynman phonons $\varepsilon_0(k)$ replaced by the self-consistent solution of Eq. (6.2). Then, the energy denominator in Eq. (4.10) in the relevant energy/momentum regime can be represented by

$$\hbar\omega - \varepsilon(p) - \varepsilon(\mathbf{k}-\mathbf{p}). \tag{6.3}$$

At long wavelengths, $\varepsilon(k)$ is monotonic and almost linear. The combination $[\varepsilon(p) + \varepsilon(\mathbf{k}-\mathbf{p})]$ has, as a function of $\mathbf{p}$, an extremum at $\mathbf{p} = \mathbf{k}/2$ with the value $2\,\varepsilon(k/2)$. Moreover, if the dispersion relation $\varepsilon(k)$ bends upwards, we have $2\,\varepsilon(k/2) < \varepsilon(k)$ and the collective mode is dampened; this is a well-known consequence of anomalous dispersion. However, *independent* of the sign of $\varepsilon''(k/2)$, the self-energy has, for $\hbar\omega \to \varepsilon(k/2)$, the behavior [37]

$$\Sigma(k,\hbar\omega) = -\frac{|V_3(\mathbf{k};-\mathbf{k}/2,-\mathbf{k}/2)|^2 k}{16\pi\rho\varepsilon'(k/2)}\sqrt{\frac{2\varepsilon(k/2)-\hbar\omega}{\varepsilon''(k/2)}}. \tag{6.4}$$

Equation (6.4) is normally used to estimate the lifetime of a phonon in the regime of anomalous dispersion $\varepsilon''(k/2) > 0$. However, the nonanalytic square-root dependence on the energy persists for $\varepsilon''(k/2) < 0$ and is visible as long as the $\varepsilon''(k/2)$ is small, in other words, up to about twice the wave number for which the dispersion relation $\varepsilon(k)$ is to a good approximation linear. This feature is seen very clearly especially in the low-density cases shown in Fig. 10. We are not aware of published experimental data that show this feature,

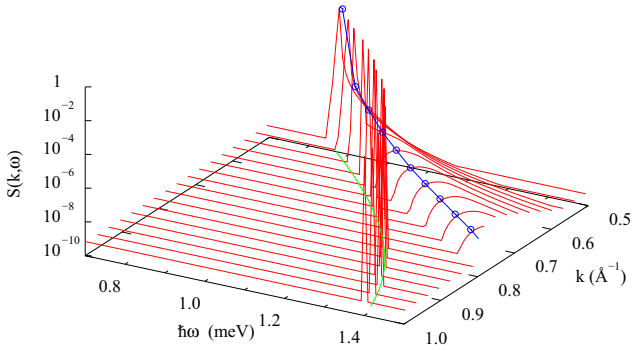

FIG. 18. (Color online) The figure shows long-wavelength results for $S(k,\hbar\omega)$ at $\rho = 0.022$ Å^{-3} at the level of BW perturbation theory (5.3) in the wave-number regime 0.5 Å^{-1} $< k <$ 1 Å^{-1} and energy range 0.7 meV $< E <$ 1.5 meV. The solid red lines are cuts of $S(k,\hbar\omega)$ for fixed wave number, the green line in the ω-k plane is the Feynman spectrum $\varepsilon_0(k)$, and the blue line is the boundary $\hbar\omega_c(k)$ of the continuum. Note the logarithmic scale and the fact that the results have been broadened to avoid δ functions and discontinuities.

but most recent high-precision neutron scattering experiments display the same effect [76].

Figure 18 shows this situation in the BW approximation for a density $\rho = 0.0220$ Å^{-3}, i.e., practically at SVP. We see a sharp collective phonon mode with normal dispersion, and above that the onset of a continuum. The collective mode and the continuum are separated by an area of zero strength. When multiparticle excitations are included, this area is filled out, but some strength remains along the line $\hbar\omega_c(k) = \hbar ck$. This is clearly seen in Fig. 19 and, of course, also in Figs. 10(a)–10(d) for $k <$ 1 Å^{-1}.

The same mechanism of mode-mode coupling is at work at the much more frequently discussed "Pitaevskii-plateau" [19]. Assuming, for the sake of discussion, a sharp phonon-roton spectrum as in the energy denominator of Eq. (5.3), the condition for the decay of an excitation into two rotons is $\omega > 2\Delta_R$.

Three observations are made:

(i) The collective mode actually bends over below the plateau and is seen, for quite some momentum regime, as a well-defined excitation. This is largely consistent with the observations of Refs. [7,29] at large momenta who also observe a gradual bending of the dispersion relation and not an abrupt "kink." It is also consistent with the theoretical work and data analysis of Pistolesi [12,13]; see also Ref. [14].

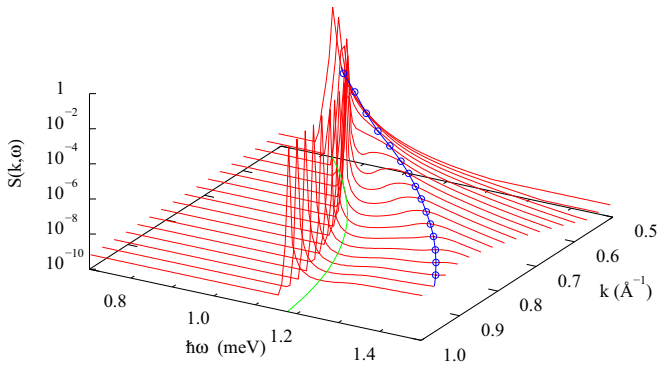

FIG. 19. (Color online) Same as Fig. 18 for the full solution of the equations of motion. The area between the phonon spectrum and $\hbar\omega_c(k)$ has been filled by multiparticle contributions, but the strength along the line $\hbar\omega_c(k)$ is also clearly visible.

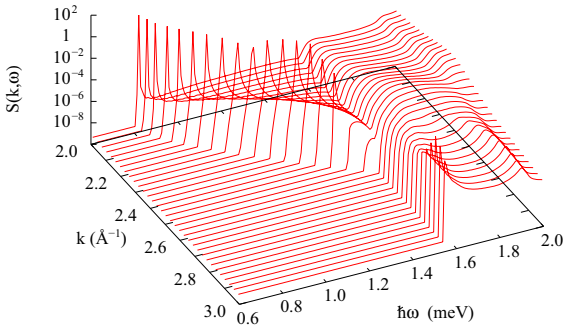

FIG. 20. (Color online) The figure shows a closeup of the dynamic structure function for the density $\rho = 0.0226$ Å^{-3}, in the wave-number regime 2 Å^{-1} $< k <$ 3 Å^{-1} and energy range 0.6 meV $< E <$ 2.0 meV. The solid red lines are cuts of $S(k,\hbar\omega)$ for fixed wave number. Note the logarithmic scale and the fact that the results have been broadened to avoid δ functions and discontinuities.

(ii) Second, we see that the plateau has an extension into the continuum for larger wavelengths. Figure 20 shows a closeup of the $S(k,\hbar\omega)$ at $\rho = 0.0226$ Å^{-3} for 2 Å^{-1} $\leqslant k \leqslant$ 3 Å^{-1}. We see clearly how the collective mode is separated from the continuum and that the plateau can be continued towards longer wavelengths. The effect becomes stronger with increasing density.

(iii) At the very highest density, the energy of the maxon is above that of the plateau, and hence a similar effect as the plateau is observed at long wavelengths. In fact, at the density $\rho = 0.026$ Å^{-3}, the plateau is very pronounced practically down to $k \approx 0.5$ Å^{-1}.

Finally, we return to the above-mentioned strength above the maxon. This feature stems from the possibility that a mode decays into a maxon and a roton. We represent the maxon energy in a form similar to Eq. (1.7):

$$\varepsilon_M(k) = \Delta_M + \frac{\hbar^2}{2\mu_M}(k - k_M)^2, \tag{6.5}$$

where Δ_M, k_M and μ_M are the maxon energy, wave number μ_R the so-called mass, respectively. We have fitted the form (6.5) to the data of Ref. [8]; the fit is shown in Fig. 17. The threshold energy for a mode decaying into a maxon and a roton under energy and momentum conservation is, for given momentum transfer $k = q - p$,

$$\hbar\omega_{M\text{-}R}(k) = \Delta_R + \Delta_M + \frac{\hbar^2}{2(\mu_R + \mu_M)}(k - k_R + k_M)^2. \tag{6.6}$$

This model is valid for $k \approx k_R - k_M$. The line $\hbar\omega_{M\text{-}R}(k)$ is also drawn in Fig. 17, showing that the feature in the spectrum is indeed due to maxon-roton coupling.

All of these effects have rather simple kinematic causes. The analytic analysis of these effects is somewhat complicated (see Supplemental Material [78]). Our results on the structural

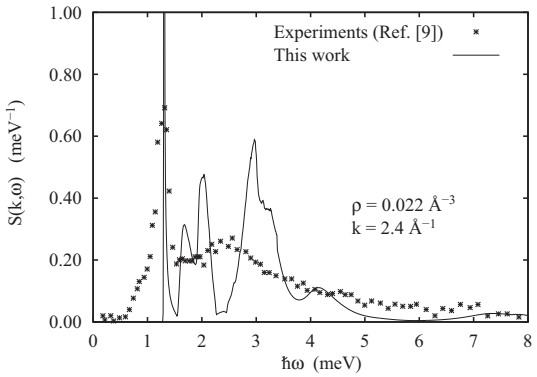

FIG. 21. The figure shows a comparison between our $S(k,\hbar\omega)$ (solid line) and the experimental one [9] (stars) at a momentum transfer of $k = 2.4$ Å^{-1}. The experimental values have been normalized to satisfy the m_0 sum rule.

properties of ^{4}He are quite encouraging. But, it should be clear that all approximations become more delicate at higher densities. Therefore, whether the appearance of a plateau below the maxon will happen at exactly the predicted density, or at a somewhat lower or higher density, is not completely determined by our theoretical calculations. The experimental data at the pressure of 2 MPa [8] indicate a maxon energy of 1.3 meV, which is close to twice the roton energy of 0.636 meV. Our theoretical results are consistent with this; therefore, one should expect that a plateau will appear around a pressure of 2 MPa.

There is also some interest in the form of the spectrum at higher energies and wave numbers (see, e.g., Ref. [9]). At higher energies, multiparticle processes become increasingly important and, because of the multitude of processes, it becomes impossible to disentangle the physics. Our approach has included all processes where a phonon splits into two phonons, which may again split, etc., but eventually they recombine into the same phonon (see Fig. 4). Processes such as the one shown in Fig. 5 are not included. Since all of these have a different kinematics, one would expect that the multitude of all multiparticle excitations have the tendency to smooth the spectrum out. This is actually seen quite well in Figs. 21 and 22:

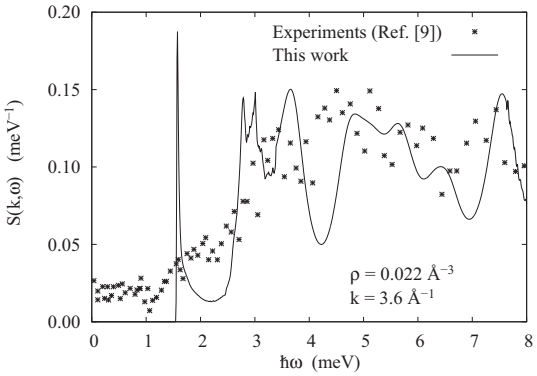

FIG. 22. Same as Fig. 21 for a momentum transfer of $k = 3.6$ Å^{-1}. The experimental values have been normalized to generate rough overall agreement with our theoretical results.

Our theoretical values show, as expected, more structure than the experiments, but the overall strength distribution is the same.

There are also experimental data at higher pressures [7]; our conclusion on these data is the same. The overall strength distribution is reasonably well represented by our theory, but because of the multitude of different excitations and decay channels, it is impossible to identify individual physical mechanisms. Therefore, we refrain from a further discussion of these data.

We conclude this section with a brief discussion on the new physics described by multiparticle fluctuations compared to earlier work containing only pair fluctuations. We stress here that these findings are generically due to multiparticle fluctuations and not due to the approximation for the two-phonon hybridization vertex (4.11); the reader is reminded that a full HNC evaluation of the self-energy at the two-body fluctuation level [4] leads to negligible improvement of the description of the dynamics.

Technically, the essential improvement of the dynamics is due to the self-consistency between the self-energy on the left-hand side of (4.10) and the energy denominator. While such a self-consistency could be expected, the precise form of the energy/momentum dependence of the self-energy must be determined from the equations of motion or by the summation of sufficiently high-order BW diagrams as carried out in Eq. (5.4).

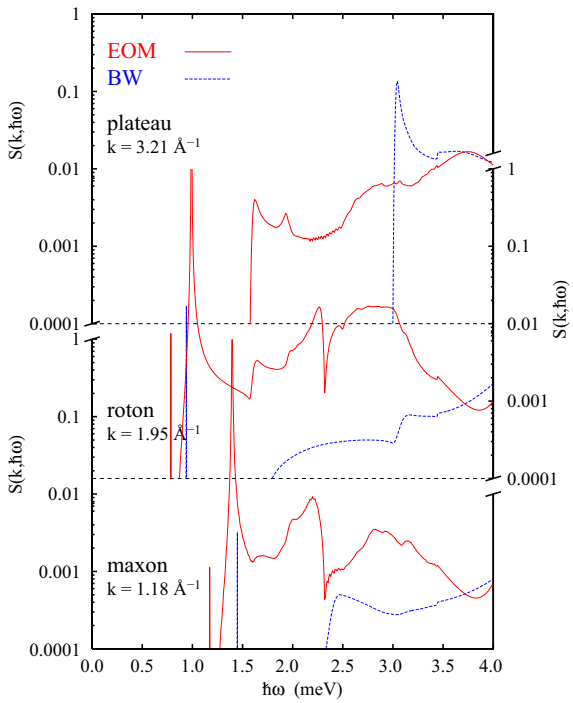

FIG. 23. (Color online) The figure compares results for $S(k,\hbar\omega)$ in BW approximation [43–46] (blue, dashed lines) with the present calculation (red, solid lines) at the density $\rho = 0.022$ Å^{-3}. We show three different momentum transfers corresponding to the maxon ($k = 1.18$ Å^{-1}, lower panel), roton ($k = 1.95$ Å^{-1}, middle panel), and the plateau region ($k = 3.21$ Å^{-1}, upper panel). The scale on the right-hand side of the plot corresponds to the roton.

Figure 23 shows a comparison of second-order BW perturbation theory and the self-consistent solution of the equations of motion. Two effects are most visible: the BW calculation for the maxon and the roton predicts a large area between the collective mode and the onset of the continuum where $S(k,\hbar\omega)$ is zero. This is because the energy where the continuum begins is determined by the energy denominator which is, in BW approximation, the Feynman spectrum (1.5). The same effect is even more visible in the energy of the plateau (upper panel of Fig. 23) which is, in BW approximation, given by twice the roton energy in Feynman approximation and not of the self-consistent spectrum.

ACKNOWLEDGMENTS

This work was supported, in part, by the Austrian Science Fund FWF under Projects No. P21264 and No. I602 and the College of Arts and Sciences of the University at Buffalo, SUNY, and from the Qatar National Research Fund No. NPRP 5 - 674 - 1 - 114. Discussions with F. Gasparini and J. Boronat are gratefully acknowledged. We thank especially H. Godfrin for valuable comments and giving us access to yet unpublished data. We also thank K. Andersen and IOP Publishing for permission to reproduce their data in Fig. 17.

APPENDIX A: EVALUATION OF THE LAGRANGIAN

1. One-body current

The quantity of interest is the term in Eq. (2.13) that contains three-body fluctuations. The triplet distribution function is generally a functional of $\rho_1(\mathbf{r}_i)$, $g_2(\mathbf{r}_i,\mathbf{r}_j)$ and triplet as well as possible higher-order ground-state correlations. We prove here that $\mathbf{W}_3(\mathbf{r};\mathbf{r}_1,\mathbf{r}_2,\mathbf{r}_3)$ is zero for the special case that the ground state contains no three-body correlations, i.e., for a Jastrow wave function. In this case, the three-body distribution function is a functional of correlation bonds $h_2(\mathbf{r}_1,\mathbf{r}_j)$ and one-body densities $\rho_1(\mathbf{r}_i)$ [59].

We carry out the proof diagrammatically. It is instructive to begin by writing the three-body distribution function in the Abe form

$$g_3(\mathbf{r}_1,\mathbf{r}_2,\mathbf{r}_3) = g_2(\mathbf{r}_1,\mathbf{r}_2)g_2(\mathbf{r}_1,\mathbf{r}_3)g_2(\mathbf{r}_2,\mathbf{r}_3)\exp[A(\mathbf{r}_1,\mathbf{r}_2,\mathbf{r}_3)]. \tag{A1}$$

$A(\mathbf{r}_1,\mathbf{r}_2,\mathbf{r}_3)$ is represented by the sum of all three-point diagrams in terms of two-particle bonds $h_2(\mathbf{r}_i,\mathbf{r}_j)$ and points $\rho_1(\mathbf{r}_i)$ that (a) have a path between each pair of external points, and (b) cannot be factorized in products of functions of the external points. A few diagrams are shown in Fig. 24.

Inserting the Abe expansion (A1) in $\mathbf{W}_3(\mathbf{r};\mathbf{r}_1,\mathbf{r}_2,\mathbf{r}_3)$ gives a new representation

$$\mathbf{W}_3(\mathbf{r};\mathbf{r}_1,\mathbf{r}_2,\mathbf{r}_3) = g_3(\mathbf{r}_1,\mathbf{r}_2,\mathbf{r}_3)\Bigg[\frac{\delta(\mathbf{r}_1-\mathbf{r})}{\rho_1(\mathbf{r})}\nabla_{\mathbf{r}}A(\mathbf{r},\mathbf{r}_2,\mathbf{r}_3) + \text{cycl.} - \frac{2}{\rho_1(\mathbf{r})}\int d^3r'\nabla_{\mathbf{r}}g_2(\mathbf{r},\mathbf{r}')\frac{\delta A(\mathbf{r}_1,\mathbf{r}_2,\mathbf{r}_3)}{\delta g_2(\mathbf{r},\mathbf{r}')}\Bigg|_{\rho_1} + \nabla_{\mathbf{r}}\frac{\delta A(\mathbf{r}_1,\mathbf{r}_2,\mathbf{r}_3)}{\delta\rho_1(\mathbf{r})}\Bigg|_{g_2}\Bigg]. \tag{A2}$$

With that, we have eliminated all contributions to $\mathbf{W}_3(\mathbf{r};\mathbf{r}_1,\mathbf{r}_2,\mathbf{r}_3)$ that contain functions of the kind $\nabla_r g_2(\mathbf{r},\mathbf{r}')$ where both $\mathbf{r}$ and $\mathbf{r}'$ are among the points $\mathbf{r}_1$, $\mathbf{r}_2$, and $\mathbf{r}_3$. In particular, the representation in terms of the Abe expansion demonstrates that the $\mathbf{W}_3(\mathbf{r};\mathbf{r}_1,\mathbf{r}_2,\mathbf{r}_3)$ is zero in the Kirkwood superposition approximation

$$g_3^{\mathrm{KSA}}(\mathbf{r}_1,\mathbf{r}_2,\mathbf{r}_3) = g_2(\mathbf{r}_1,\mathbf{r}_2)g_2(\mathbf{r}_1,\mathbf{r}_3)g_2(\mathbf{r}_2,\mathbf{r}_3). \tag{A3}$$

This should serve to make the exact result more plausible.

It remains to prove that

$$\frac{\delta(\mathbf{r}_1-\mathbf{r})}{\rho_1(\mathbf{r})}\nabla_{\mathbf{r}}A(\mathbf{r},\mathbf{r}_2,\mathbf{r}_3) + \text{cycl.} - \frac{2}{\rho_1(\mathbf{r})}\int d^3r'\nabla_{\mathbf{r}}g_2(\mathbf{r},\mathbf{r}')\frac{\delta A(\mathbf{r}_1,\mathbf{r}_2,\mathbf{r}_3)}{\delta g_2(\mathbf{r},\mathbf{r}')}\Bigg|_{\rho_1} = -\nabla_{\mathbf{r}}\frac{\delta A(\mathbf{r}_1,\mathbf{r}_2,\mathbf{r}_3)}{\delta\rho_1(\mathbf{r})}\Bigg|_{g_2}. \tag{A4}$$

The expression (A4) can be represented by a diagrammatic expansion in terms of correlation bonds $h_2(\mathbf{r}_i\mathbf{r}_j)$, *one* bond $\nabla_{\mathbf{r}}g_2(\mathbf{r},\mathbf{r}_i)$, and internal points $\rho(\mathbf{r}_i)$.

The term

$$-\frac{2}{\rho_1(\mathbf{r})}\int d^3r'\nabla_{\mathbf{r}}g_2(\mathbf{r},\mathbf{r}')\frac{\delta A(\mathbf{r}_1,\mathbf{r}_2,\mathbf{r}_3)}{\delta g_2(\mathbf{r},\mathbf{r}')}\Bigg|_{\rho_1} \tag{A5}$$

is obtained as follows:

(a) open, in turn, each *pair of points* $(\mathbf{r}_i,\mathbf{r}_j)$ that is connected by a correlation line;

(b) replace $h_2(\mathbf{r}_i,\mathbf{r}_j)$ by $\frac{1}{2}[\nabla_i g_2(\mathbf{r}_i,\mathbf{r}_j) + \nabla_j g_2(\mathbf{r}_i,\mathbf{r}_j)]$;

(c) close each point where no gradient acts, call the point left open $\mathbf{r}$;

(d) collect all diagrams; the nonintegrated points are of the form $[\nabla g_2(\mathbf{r},\mathbf{r}_i)]h_2(\mathbf{r},\mathbf{r}_j)h_2(\mathbf{r},\mathbf{r}_k) + h_2(\mathbf{r},\mathbf{r}_i)[\nabla g_2(\mathbf{r},\mathbf{r}_j)]h_2(\mathbf{r},\mathbf{r}_k) + h_2(\mathbf{r},\mathbf{r}_i)h_2(\mathbf{r},\mathbf{r}_j)[\nabla g_2(\mathbf{r},\mathbf{r}_k)] + \cdots = \nabla[h_2(\mathbf{r},\mathbf{r}_i)h_2(\mathbf{r},\mathbf{r}_j)h_2(\mathbf{r},\mathbf{r}_k)\cdots]$.

Two types of diagrams appear: Those where the point $\mathbf{r}$ is one of the external points $\mathbf{r}_1$, $\mathbf{r}_2$, or $\mathbf{r}_3$ and those where it is not. The first type of diagrams is canceled against the first term in Eq. (A4). Thus, in the second step we have proven that there is no contribution to $\mathbf{W}_3(\mathbf{r};\mathbf{r}_1,\mathbf{r}_2,\mathbf{r}_3)$ where $\mathbf{r}$ is the same as one of the coordinates $\mathbf{r}_1$, $\mathbf{r}_2$, or $\mathbf{r}_3$.

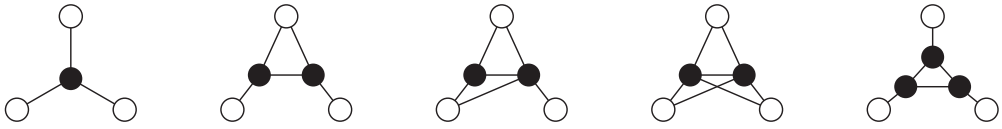

FIG. 24. The figure shows a few low-order diagrams contributing to the Abe function $A(\mathbf{r}_1,\mathbf{r}_2,\mathbf{r}_3)$.

Finally, the term on the right-hand side of Eq. (A4) is evaluated as follows:

(a) open in turn each internal point; label this point with $\mathbf{r}$;

(b) apply the gradient at this point;

(c) since only $h_2(\mathbf{r},\mathbf{r}_j)$ bonds are attached to the open point, but no density factor, we get $\nabla[h_2(\mathbf{r},\mathbf{r}_i)h_2(\mathbf{r},\mathbf{r}_j)h_2(\mathbf{r},\mathbf{r}_k)\ldots]$ (note that $\mathbf{r}$ is an internal point).

This is exactly the same as what we got from the variation $\delta A(\mathbf{r}_1,\mathbf{r}_2,\mathbf{r}_3)/\delta g_2(\mathbf{r},\mathbf{r}')$ where $\mathbf{r}$ is one of the internal points. Thus, the two expressions on the left- and the right-hand sides of Eq. (A4) are the same

2. Time-derivative term

We must rewrite the variations with respect to the $\delta u_n(t)$ in terms of variations with respect to the $\delta v_n(t)$. In a somewhat shorthand notation, we have

$$\begin{aligned}
\frac{\delta}{\delta v_1} &= \frac{\delta u_1}{\delta v_1}\frac{\delta}{\delta u_1} = \frac{\delta}{\delta u_1},\\
\frac{\delta}{\delta v_2} &= \frac{\delta u_2}{\delta v_2}\frac{\delta}{\delta u_2} + \frac{\delta u_1}{\delta v_2}\frac{\delta}{\delta u_1} = \frac{\delta}{\delta u_2} + \frac{\delta u_1}{\delta v_2}\frac{\delta}{\delta u_1},\\
\frac{\delta}{\delta v_3} &= \frac{\delta u_3}{\delta v_3}\frac{\delta}{\delta u_3} + \frac{\delta u_2}{\delta v_3}\frac{\delta}{\delta u_2} + \frac{\delta u_1}{\delta v_3}\frac{\delta}{\delta u_1} = \frac{\delta}{\delta u_3} + \frac{\delta u_2}{\delta v_3}\frac{\delta}{\delta u_2} + \frac{\delta u_1}{\delta v_3}\frac{\delta}{\delta u_1}.
\end{aligned} \tag{A6}$$

Consequently,

$$\begin{aligned}
\frac{\delta\mathcal{L}_t(t)}{\delta u_1^*(\mathbf{r}_1;t)} &= -\frac{i\hbar}{4}\delta\dot{\rho}(\mathbf{r}_1;t),\\
\frac{\delta\mathcal{L}_t(t)}{\delta v_2^*(\mathbf{r}_1,\mathbf{r}_2;t)} &= \frac{i\hbar}{8}\left[\dot{\rho}_2(\mathbf{r}_1,\mathbf{r}_2;t) - \rho_1(\mathbf{r}_1)g_2(\mathbf{r}_1,\mathbf{r}_2)\dot{\rho}_1(\mathbf{r}_2;t) - \rho_1(\mathbf{r}_2)g_2(\mathbf{r}_1,\mathbf{r}_2)\dot{\rho}_1(\mathbf{r}_1;t) - \rho_1(\mathbf{r}_1)\rho_1(\mathbf{r}_2)\int d^3r_3\frac{\delta g_2(\mathbf{r}_1,\mathbf{r}_2)}{\delta\rho_1(\mathbf{r}_3)}\dot{\rho}_1(\mathbf{r}_3;t)\right]\\
&= \frac{i\hbar}{8}\rho_1(\mathbf{r}_1)\rho_1(\mathbf{r}_2)\int d^3r_3d^3r_4\frac{\delta g_2(\mathbf{r}_1,\mathbf{r}_2;t)}{\delta u_2(\mathbf{r}_3,\mathbf{r}_4)}\delta\dot{v}_2(\mathbf{r}_3,\mathbf{r}_4;t).
\end{aligned} \tag{A7}$$

The calculation of the three-body term is lengthier but straightforward:

$$\begin{aligned}
\frac{\delta\mathcal{L}_t(t)}{\delta v_3^*(\mathbf{r}_1,\mathbf{r}_2,\mathbf{r}_3;t)} &= -\frac{i\hbar}{24}\left\{\dot{\rho}_3(\mathbf{r}_1,\mathbf{r}_2,\mathbf{r}_3;t) - \int d^3r_4d^3r_5\frac{\delta\rho_3(\mathbf{r}_1,\mathbf{r}_2,\mathbf{r}_3)}{\delta g_2(\mathbf{r}_4,\mathbf{r}_5)}\frac{\delta\dot{\rho}_2(\mathbf{r}_4,\mathbf{r}_5)}{\rho_1(\mathbf{r}_4)\rho_1(\mathbf{r}_5)}\right.\\
&\quad\left. - \int d^3r_6\left[\frac{\delta\rho_3(\mathbf{r}_1,\mathbf{r}_2,\mathbf{r}_3)}{\delta\rho_1(\mathbf{r}_6)} - \int d^3r_4d^3r_5\frac{\delta\rho_2(\mathbf{r}_4,\mathbf{r}_5)}{\rho_1(\mathbf{r}_4)\rho_1(\mathbf{r}_5)\delta\rho_1(\mathbf{r}_6)}\frac{\delta\rho_3(\mathbf{r}_1,\mathbf{r}_2,\mathbf{r}_3)}{\delta g_2(\mathbf{r}_4,\mathbf{r}_5)}\right]\delta\dot{\rho}_1(\mathbf{r}_6;t)\right\}\\
&= -\frac{i\hbar}{24}\rho_1(\mathbf{r}_1)\rho_1(\mathbf{r}_2)\rho_1(\mathbf{r}_3)\int d^3r_4d^3r_5d^3r_6\frac{\delta g_3(\mathbf{r}_1,\mathbf{r}_2,\mathbf{r}_3;t)}{\delta u_3(\mathbf{r}_4,\mathbf{r}_5,\mathbf{r}_6)}\delta\dot{v}_3(\mathbf{r}_4,\mathbf{r}_5,\mathbf{r}_6;t).
\end{aligned} \tag{A8}$$

Thus, our choice of independent variables diagonalizes the time-derivative term, and we can summarize our result in the form (3.6).

3. Interaction Lagrangian

The original form of the interaction part of the Lagrangian is

$$\begin{aligned}
\mathcal{L}_{\rm int}^{(1,1)}(t) &= \frac{\hbar^2}{8m}\int d^3\rho_1|\nabla\delta u_1(\mathbf{r}_1;t)|^2,\\
\mathcal{L}_{\rm int}^{(1,2)}(t) &= \frac{\hbar^2}{8m}\int d^3\rho_1d^3\rho_2g_2(\mathbf{r}_1,\mathbf{r}_2)\nabla_1\delta u_1(\mathbf{r}_1;t)\cdot\nabla_1\delta u_2^*(\mathbf{r}_1,\mathbf{r}_2),\\
\mathcal{L}_{\rm int}^{(1,3)}(t) &= \frac{\hbar^2}{16m}\int d^3\rho_1d^3\rho_2d^3\rho_3g_3(\mathbf{r}_1,\mathbf{r}_2,\mathbf{r}_3)\nabla_1\delta u_1(\mathbf{r}_1;t)\cdot\nabla_1\delta u_3^*(\mathbf{r}_1,\mathbf{r}_2,\mathbf{r}_3;t),\\
\mathcal{L}_{\rm int}^{(2,2)}(t) &= \frac{\hbar^2}{8m}\int d^3\rho_1d^3\rho_2g_2(\mathbf{r}_1,\mathbf{r}_2)|\nabla_1\delta u_2(\mathbf{r}_1,\mathbf{r}_2;t)|^2\\
&\quad+\frac{\hbar^2}{8m}\int d^3\rho_1d^3\rho_2d^3\rho_3g_3(\mathbf{r}_1,\mathbf{r}_2,\mathbf{r}_3)\nabla_1\delta u_2(\mathbf{r}_1,\mathbf{r}_2;t)\nabla_1\delta u_2^*(\mathbf{r}_1,\mathbf{r}_3;t),\\
\mathcal{L}_{\rm int}^{(2,3)}(t) &= \frac{\hbar^2}{8m}\int d^3\rho_1d^3\rho_2d^3\rho_3g_3(\mathbf{r}_1,\mathbf{r}_2,\mathbf{r}_3)\nabla_1\delta u_2(\mathbf{r}_1,\mathbf{r}_2;t)\cdot\nabla_1\delta u_3^*(\mathbf{r}_1,\mathbf{r}_2,\mathbf{r}_3;t)\\
&\quad+\frac{\hbar^2}{16m}\int d^3\rho_1d^3\rho_2d^3\rho_3d^3\rho_4g_4(\mathbf{r}_1,\mathbf{r}_2,\mathbf{r}_3,\mathbf{r}_4)\nabla_1\delta u_2(\mathbf{r}_1,\mathbf{r}_2;t)\cdot\nabla_1\delta u_3^*(\mathbf{r}_1,\mathbf{r}_3,\mathbf{r}_4;t),
\end{aligned}$$

$$\mathcal{L}_{\rm int}^{(3,3)}(t) = \frac{\hbar^2}{16m}\int d^3\rho_1 d^3\rho_2 d^3\rho_3 g_3(\mathbf{r}_1,\mathbf{r}_2,\mathbf{r}_3)|\nabla_1\delta u_3(\mathbf{r}_1,\mathbf{r}_2,\mathbf{r}_3;t)|^2$$
$$+\frac{\hbar^2}{8m}\int d^3\rho_1 d^3\rho_2 d^3\rho_3 d^3\rho_4 g_4(\mathbf{r}_1,\mathbf{r}_2,\mathbf{r}_3,\mathbf{r}_4)\nabla_1\delta u_3(\mathbf{r}_1,\mathbf{r}_2,\mathbf{r}_3;t)\cdot\nabla_1\delta u_3^*(\mathbf{r}_1,\mathbf{r}_2,\mathbf{r}_4;t)$$
$$+\frac{\hbar^2}{32m}\int d^3\rho_1 d^3\rho_2 d^3\rho_3 d^3\rho_4 d^3 r_5 g_5(\mathbf{r}_1,\mathbf{r}_2,\mathbf{r}_3,\mathbf{r}_4,\mathbf{r}_5)\nabla_1\delta u_3(\mathbf{r}_1,\mathbf{r}_2,\mathbf{r}_3;t)\cdot\nabla_1\delta u_3^*(\mathbf{r}_1,\mathbf{r}_4,\mathbf{r}_5;t). \tag{A9}$$

We first collect all terms that contribute to the current (2.12); this moves the appearance of the one-body fluctuation $\delta u_1(\mathbf{r};t)$ into the first term in Eq. (3.10). The remaining terms are

$$\mathcal{L}_{\rm int}'^{(2,2)}(t) = \frac{\hbar^2}{8m}\int d^3\rho_1 d^3\rho_2 d^3\rho_3 \nabla_{\mathbf{r}_1}\delta u_2(\mathbf{r}_1,\mathbf{r}_2;t)\mathcal{F}_{22}(\mathbf{r}_1;\mathbf{r}_2,\mathbf{r}_3)\nabla_{\mathbf{r}_1}\delta u_2^*(\mathbf{r}_1,\mathbf{r}_3;t),$$
$$\mathcal{L}_{\rm int}'^{(2,3)}(t) = \frac{\hbar^2}{8m}\int d^3\rho_1 d^3\rho_2 d^3\rho_3 d^3\rho_4 \nabla_{\mathbf{r}_1}\delta u_2(\mathbf{r}_1,\mathbf{r}_2;t)\mathcal{F}_{23}(\mathbf{r}_1;\mathbf{r}_2,\mathbf{r}_3,\mathbf{r}_4)\nabla_{\mathbf{r}_1}\delta u_3^*(\mathbf{r}_1,\mathbf{r}_3,\mathbf{r}_4;t),$$
$$\mathcal{L}_{\rm int}'^{(3,3)}(t) = \frac{\hbar^2}{16m}\int d^3\rho_1 d^3\rho_2 d^3\rho_3 g_3(\mathbf{r}_1,\mathbf{r}_2,\mathbf{r}_3)|\nabla_{\mathbf{r}_1}\delta u_3(\mathbf{r}_1,\mathbf{r}_2,\mathbf{r}_3;t)|^2$$
$$+\frac{\hbar^2}{8m}\int d^3\rho_1 d^3\rho_2 d^3\rho_3 d^3\rho_4 g_4(\mathbf{r}_1,\mathbf{r}_2,\mathbf{r}_3,\mathbf{r}_4)\nabla_{\mathbf{r}_1}\delta u_3(\mathbf{r}_1,\mathbf{r}_2,\mathbf{r}_3;t)\cdot\nabla_{\mathbf{r}_1}\delta u_3^*(\mathbf{r}_1,\mathbf{r}_2,\mathbf{r}_4;t)$$
$$+\frac{\hbar^2}{32m}\int d^3\rho_1 d^3\rho_2 d^3\rho_3 d^3\rho_4 d^3 r_5[g_5(\mathbf{r}_1,\mathbf{r}_2,\mathbf{r}_3,\mathbf{r}_2',\mathbf{r}_3') - g_3(\mathbf{r}_1,\mathbf{r}_2,\mathbf{r}_3)g_3(\mathbf{r}_1,\mathbf{r}_2',\mathbf{r}_3')]$$
$$\times\nabla_{\mathbf{r}_1}\delta u_3(\mathbf{r}_1,\mathbf{r}_2,\mathbf{r}_3;t)\cdot\nabla_{\mathbf{r}_1}\delta u_3^*(\mathbf{r}_1,\mathbf{r}_2',\mathbf{r}_3';t) \tag{A10}$$

with [4]

$$\mathcal{F}_{22}(\mathbf{r}_1;\mathbf{r}_2,\mathbf{r}_3) \equiv g_2(\mathbf{r}_1,\mathbf{r}_2)\frac{\delta(\mathbf{r}_2-\mathbf{r}_3)}{\rho_1(\mathbf{r}_2)} + g_3(\mathbf{r}_1,\mathbf{r}_2,\mathbf{r}_3) - g_2(\mathbf{r}_1,\mathbf{r}_2)g_2(\mathbf{r}_1,\mathbf{r}_3) \tag{A11}$$

and

$$\mathcal{F}_{23}(\mathbf{r}_1;\mathbf{r}_2,\mathbf{r}_3,\mathbf{r}_4) \equiv g_3(\mathbf{r}_1,\mathbf{r}_2,\mathbf{r}_3)\frac{\delta(\mathbf{r}_2-\mathbf{r}_4)}{\rho_1(\mathbf{r}_2)} + \frac{1}{2}[g_4(\mathbf{r}_1,\mathbf{r}_2,\mathbf{r}_3,\mathbf{r}_4) - g_2(\mathbf{r}_1,\mathbf{r}_2)g_2(\mathbf{r}_1,\mathbf{r}_3,\mathbf{r}_4)]. \tag{A12}$$

Note that

$$\frac{\delta g_2(\mathbf{r}_1,\mathbf{r}_3)}{\delta u_2(\mathbf{r}_1,\mathbf{r}_2)} = \rho_1(\mathbf{r}_2)\mathcal{F}_{22}(\mathbf{r}_1;\mathbf{r}_2,\mathbf{r}_3) \tag{A13}$$

and

$$\frac{\delta g_3(\mathbf{r}_1,\mathbf{r}_3,\mathbf{r}_4)}{\delta u_2(\mathbf{r}_1,\mathbf{r}_2)} = \rho_1(\mathbf{r}_1)[\mathcal{F}_{23}(\mathbf{r}_1;\mathbf{r}_2,\mathbf{r}_3,\mathbf{r}_4) + \mathcal{F}_{23}(\mathbf{r}_1;\mathbf{r}_2,\mathbf{r}_4,\mathbf{r}_3)]. \tag{A14}$$

The new aspect compared with earlier derivations is that we also eliminate $\delta u_2(\mathbf{r}_1,\mathbf{r}_i;t)$ in favor of $\delta v_2(\mathbf{r}_1,\mathbf{r}_i;t)$. Inserting Eq. (2.10) into (A10) generates a number of terms containing derivatives of the triplet fluctuations and derivatives of distribution functions. The manipulations are somewhat tedious but straightforward. Here, we spell out only one key step: One of the terms occurring is of the form

$$\int d^3\rho_2' d^3\rho_3'\Big[\int d^3\rho_1' d^3\rho_2'' \mathcal{F}_{22}(\mathbf{r}_1;\mathbf{r}_2,\mathbf{r}_2'')\nabla_{\mathbf{r}_1}[\mathcal{G}_{23}(\mathbf{r}_1,\mathbf{r}_2'';\mathbf{r}_1'\mathbf{r}_2'\mathbf{r}_3')\delta v_3(\mathbf{r}_1',\mathbf{r}_2',\mathbf{r}_3')] - \mathcal{F}_{23}(\mathbf{r}_1;\mathbf{r}_2,\mathbf{r}_2',\mathbf{r}_3')\nabla_{\mathbf{r}_1}\delta v_3(\mathbf{r}_1,\mathbf{r}_2',\mathbf{r}_3')\Big]$$
$$= \int d^3\rho_1' d^3\rho_2' d^3\rho_3'\delta v_3(\mathbf{r}_1',\mathbf{r}_2',\mathbf{r}_3')\int d^3\rho_2'' \mathcal{F}_{22}(\mathbf{r}_1;\mathbf{r}_2,\mathbf{r}_2'')\nabla_{\mathbf{r}_1}\mathcal{G}_{23}(\mathbf{r}_1,\mathbf{r}_2'';\mathbf{r}_1',\mathbf{r}_2',\mathbf{r}_3')$$
$$+\int d^3\rho_2' d^3\rho_3'\nabla_{\mathbf{r}_1}\delta v_3(\mathbf{r}_1,\mathbf{r}_2',\mathbf{r}_3')\Big[\int d^3\rho_2'' \mathcal{F}_{22}(\mathbf{r}_1;\mathbf{r}_2,\mathbf{r}_2'')\frac{1}{2}\frac{\delta g_3(\mathbf{r}_1,\mathbf{r}_2',\mathbf{r}_3')}{\delta g_2(\mathbf{r}_1,\mathbf{r}_2'')} - \mathcal{F}_{23}(\mathbf{r}_1;\mathbf{r}_2,\mathbf{r}_2',\mathbf{r}_3')\Big]. \tag{A15}$$

The terms in the square brackets cancel due to the properties (A13) and (A14) which leads to the form (3.12)–(3.14) of the Lagrangian, note that there is a symmetry factor $\frac{3}{2}$ compared to Eq. (2.11) because the coordinate $\mathbf{r}_1$ is the same in the numerator

and the denominator. The coefficient function in $\mathcal{L}''^{(3,3)}_{\rm int}(t)$ is

$$\mathcal{F}_{33}(\mathbf{r}_1;\mathbf{r}_2,\mathbf{r}_3;\mathbf{r}'_2,\mathbf{r}'_3) = g_3(\mathbf{r}_1,\mathbf{r}_2,\mathbf{r}_3)\frac{\delta(\mathbf{r}_2-\mathbf{r}'_2)}{\rho_1(\mathbf{r}_2)}\frac{\delta(\mathbf{r}_3-\mathbf{r}'_3)}{\rho_1(\mathbf{r}_3)} + 2g_4(\mathbf{r}_1,\mathbf{r}_2,\mathbf{r}_3,\mathbf{r}'_3)\frac{\delta(\mathbf{r}_2-\mathbf{r}'_2)}{\rho_1(\mathbf{r}_2)}$$
$$+\frac{1}{2}[g_5(\mathbf{r}_1,\mathbf{r}_2,\mathbf{r}_3,\mathbf{r}'_2,\mathbf{r}'_3) - g_3(\mathbf{r}_1,\mathbf{r}_2,\mathbf{r}_3)g_3(\mathbf{r}_1,\mathbf{r}'_2,\mathbf{r}'_3)]$$
$$-2\int d^3\rho''_2 d^3\rho''_3 \mathcal{G}_{32}(\mathbf{r}_1,\mathbf{r}_2,\mathbf{r}_3;\mathbf{r}_1,\mathbf{r}''_2)\mathcal{F}_{22}(\mathbf{r}_1;\mathbf{r}''_2,\mathbf{r}''_3)\mathcal{G}_{23}(\mathbf{r}_1,\mathbf{r}''_3;\mathbf{r}_1,\mathbf{r}'_2,\mathbf{r}'_3). \quad \text{(A16)}$$

APPENDIX B: DERIVATION OF THE RESPONSE FUNCTION

As already mentioned above, there is practically no advantage in assuming a uniform geometry for the derivation of the response function. Consequently, we proceed here with a completely general formulation that is also applicable in nonuniform geometries such as films and clusters. We restrict ourselves, however, to a formulation that leads to the so-called "unrenormalized" form of the self-energy [4]. The renormalized form includes specific sets of higher-order diagrams that can be summed easily. However, our earlier work led to the conclusion that one must *consistently* calculate at least the HNC class of diagrams in *all* ingredients due to canceling errors. We will, however, point out which terms should be kept to obtain the "renormalized" form of the self-energy.

In a nonuniform geometry, we introduce the "tilde" notation [42]

$$\tilde{F}(\mathbf{r}_1,\ldots,\mathbf{r}_n) = \sqrt{\rho_1(\mathbf{r}_1)\ldots\rho_1(\mathbf{r}_n)}F(\mathbf{r}_1,\ldots,\mathbf{r}_n). \quad \text{(B1)}$$

It is advantageous to expand all quantities in terms of Feynman phonon states. These are defined by the generalized eigenvalue problem

$$H_1(\mathbf{r})\psi_n(\mathbf{r}) = \hbar\omega_n\int d^3r'\tilde{S}(\mathbf{r},\mathbf{r}')\psi_n(\mathbf{r}') = \hbar\omega_n\phi_n(\mathbf{r}), \quad \text{(B2)}$$

where

$$H_1(\mathbf{r}) = -\frac{\hbar^2}{2m}\frac{1}{\sqrt{\rho_1(\mathbf{r})}}\nabla\rho_1(\mathbf{r})\cdot\nabla\frac{1}{\sqrt{\rho_1(\mathbf{r})}}. \quad \text{(B3)}$$

The states $\psi_n(\mathbf{r})$ and their adjoints $\phi_n(\mathbf{r})$ satisfy the orthogonality and closure relations

$$(\psi_n|H_1|\psi_m) = \hbar\omega_n\delta_{m,n}, \quad \text{(B4)}$$
$$\sum_n \psi_n(\mathbf{r}_1)\phi_n(\mathbf{r}_2) = \delta(\mathbf{r}_1-\mathbf{r}_2),$$
$$\sum_n \phi_n(\mathbf{r}_1)\phi_n(\mathbf{r}_2) = \tilde{S}(\mathbf{r}_1,\mathbf{r}_2) \quad \text{(B5)}$$

and expand the fluctuating amplitudes in terms of the Feynman states

$$\delta v^{(i)}_{m_1,\ldots m_i} = \int d^3r_1\ldots d^3r_i\phi^*_{m_1}(\mathbf{r}_1)\ldots\phi^*_{m_i}(\mathbf{r}_i)\delta\tilde{v}_i(\mathbf{r}_1,\ldots,\mathbf{r}_i). \quad \text{(B6)}$$

We first deal with the three-body equation. From the variation of the Lagrangian we get

$$\int d^3r'_1 d^3r'_2 d^3r'_3 \tilde{\mathcal{E}}_{33}(\mathbf{r}_1,\mathbf{r}_2,\mathbf{r}_3;\mathbf{r}'_1,\mathbf{r}'_2,\mathbf{r}'_3;\pm\omega)\delta\tilde{v}^{(\pm)}_3(\mathbf{r}'_1,\mathbf{r}'_2,\mathbf{r}'_3,\hbar\omega) \quad \text{(B7)}$$
$$= -\frac{\hbar^2}{2m}\int d^3r''_1 d^3r'_2\frac{1}{\sqrt{\rho_1(\mathbf{r}''_1)}}\tilde{\mathcal{F}}_{22}(\mathbf{r}''_1;\mathbf{r}_1,\mathbf{r}'_2)\tilde{\mathbf{W}}_2(\mathbf{r}''_1;\mathbf{r}_2,\mathbf{r}_3)$$
$$\cdot\delta\tilde{\mathbf{Q}}^{(\pm)}(\mathbf{r}''_1,\mathbf{r}'_2) + \text{cycl.} \quad \text{(B8)}$$

with

$$\tilde{\mathcal{E}}_{nn}(\mathbf{r}_1,\ldots,\mathbf{r}_n;\mathbf{r}'_1,\ldots,\mathbf{r}'_n;\hbar\omega)$$
$$= -\frac{\hbar^2}{2m}\frac{1}{\sqrt{\rho_1(\mathbf{r}_1)}}\nabla_1\cdot[\delta(\mathbf{r}_1-\mathbf{r}'_1)\tilde{\mathcal{F}}_{nn}(\mathbf{r}_1,\ldots,\mathbf{r}_n;\ldots,\mathbf{r}'_n)]$$
$$\times\nabla'_1\frac{1}{\sqrt{\rho_1(\mathbf{r}'_1)}} + \text{cycl.} - \hbar\omega\frac{\delta\tilde{g}_n(\mathbf{r}_1,\ldots,\mathbf{r}_n)}{\delta\tilde{u}_n(\mathbf{r}'_1,\ldots,\mathbf{r}'_n)}. \quad \text{(B9)}$$

Projecting Eq. (B8) onto three states $\psi_n(\mathbf{r})$ and using the convolution approximation (4.7) we find

$$\hbar(\omega_k+\omega_m+\omega_n\mp\omega)\delta v^{(3\pm)}_{kmn}$$
$$= -\frac{\hbar^2}{2m}\int d^3r\tilde{\mathbf{W}}_{mn}(\mathbf{r})\cdot\delta\tilde{\mathbf{Q}}^{(\pm)}_k(\mathbf{r}) + \text{cycl.}, \quad \text{(B10)}$$

where

$$\tilde{\mathbf{W}}_{mn}(\mathbf{r}) = \int d^3r_2 d^3r_3\tilde{\mathbf{W}}_2(\mathbf{r};\mathbf{r}_2,\mathbf{r}_3)\psi_m(\mathbf{r}_2)\psi_n(\mathbf{r}_2) \quad \text{(B11)}$$

and

$$\delta\tilde{\mathbf{Q}}^{(\pm)}_k(\mathbf{r}) = \int d^3r_2\delta\tilde{\mathbf{Q}}^{(\pm)}(\mathbf{r},\mathbf{r}_2)\phi_k(\mathbf{r}_2). \quad \text{(B12)}$$

To obtain the unrenormalized form, we approximate the function $\delta\mathbf{Q}(\mathbf{r}_1,\mathbf{r}_2)$ in Eq. (4.5) by its first term, i.e.,

$$\delta\tilde{\mathbf{Q}}^{(\pm)}_k(\mathbf{r}) \approx \sqrt{\rho_1(\mathbf{r})}\int d^3r_2\nabla_{\mathbf{r}}\delta v^{(\pm)}_2(\mathbf{r},\mathbf{r}_2)\sqrt{\rho_1(\mathbf{r}_2)}\phi_k(\mathbf{r}_2). \quad \text{(B13)}$$

We then obtain

$$\hbar(\omega_k+\omega_m+\omega_n\mp\omega)\delta v^{(3\pm)}_{kmn} = \left[\sum_i \delta v^{(2\pm)}_{ki}V^{(i)}_{mn} + \text{cycl.}\right]. \quad \text{(B14)}$$

Above, the $V^{(i)}_{mn}$ are the three-phonon vertices known from the pair excitation theory for inhomogeneous systems [42]:

$$V^{(i)}_{mn} = \frac{\hbar^2}{2m}\int d^3r\frac{\psi_i(\mathbf{r}_1)}{\sqrt{\rho_1(\mathbf{r}_1)}}\nabla\cdot[\sqrt{\rho_1(\mathbf{r}_1)}\tilde{\mathbf{W}}_{mn}(\mathbf{r}_1)]. \quad \text{(B15)}$$

Turn now to the two-body equation. From the variation of the Lagrangian we get

$$\int d^3r_1' d^3r_2' \tilde{\mathcal{E}}_{22}(\mathbf{r}_1,\mathbf{r}_2;\mathbf{r}_1',\mathbf{r}_2';\mp\omega)\delta\tilde{v}_2^{(\pm)}(\mathbf{r}_1',\mathbf{r}_2',\hbar\omega)$$
$$-\frac{\hbar^2}{4m}\frac{1}{\sqrt{\rho_1(\mathbf{r}_1)}}\int d^3r_2' dr_2'' dr_3'' \nabla_1 \tilde{\mathcal{F}}_{22}(\mathbf{r}_1;\mathbf{r}_2,\mathbf{r}_2')\cdot\tilde{\mathbf{W}}_2(\mathbf{r}_1,\mathbf{r}_2'',\mathbf{r}_3'')\delta\tilde{v}_3^{(\pm)}(\mathbf{r}_2',\mathbf{r}_2'',\mathbf{r}_3'')+\{\mathbf{r}_1\leftrightarrow\mathbf{r}_2\}$$
$$=\frac{\hbar^2}{2m}\int d^3r_3\tilde{\mathbf{W}}_2(\mathbf{r}_3,\mathbf{r}_1,\mathbf{r}_2)\cdot\left[\sqrt{\rho_1(\mathbf{r}_3)}\nabla_3\delta v_1^{(\pm)}(\mathbf{r}_3)-\frac{1}{2}\int d^2r_1' d^3r_2'\tilde{\mathbf{W}}_2(\mathbf{r}_3,\mathbf{r}_1',\mathbf{r}_2')\delta\tilde{v}_2^{(\pm)}(\mathbf{r}_1',\mathbf{r}_2')\right]. \tag{B16}$$

The "unrenormalized" form is obtained by neglecting the last term. Projecting the equation again in the space of Feynman excitations and using the uniform limit approximation for $\tilde{\mathcal{F}}_{22}(\mathbf{r}_1;\mathbf{r}_2,\mathbf{r}_2')$ and $\tilde{\mathbf{W}}_2(\mathbf{r}_3,\mathbf{r}_1,\mathbf{r}_2)$ then gives

$$\hbar(\omega_m+\omega_n\mp\omega)\delta v_{mn}^{(2\pm)}-\frac{\hbar^2}{4m}\int d^3r\frac{\psi_m(\mathbf{r})}{\sqrt{\rho_1(\mathbf{r})}}\nabla\sqrt{\rho_1(\mathbf{r})}\sum_{ij}\tilde{\mathbf{W}}_{ij}(\mathbf{r})\delta\tilde{v}_{nij}^{(3\pm)}+\{m\leftrightarrow n\}$$
$$=\hbar(\omega_m+\omega_n\mp\omega)\delta v_{mn}^{(2\pm)}-\frac{1}{2}\sum_{ij}V_{ij}^{(m)}\delta\tilde{v}_{nij}^{(3\pm)}+\{m\leftrightarrow n\}$$
$$=\frac{\hbar^2}{2m}\int d^3r\tilde{\mathbf{W}}_{mn}(\mathbf{r})\cdot\nabla\delta v_1^{(\pm)}(\mathbf{r})=-\sum_k V_{mn}^{(k)}\delta v_k^{(1\pm)}. \tag{B17}$$

We can now insert the solution (B14) of the three-body equation in the second term on the left-hand side and recover the unrenormalized form of the self-energy

$$\frac{1}{2}\sum_{ij}V_{ij}^{(m)}\delta\tilde{v}_{nij}^{(3\pm)}=\sum_i\Sigma_{mi}^{(0)}(\hbar\omega-\hbar\omega_n)\delta v_{in}^{(2)}, \tag{B18}$$

where

$$\Sigma_{mn}^{(0)}(\hbar\omega)=\frac{1}{2}\sum_{ik}\frac{V_{ik}^{(n)}V_{ik}^{(m)}}{\hbar(\omega_i+\omega_k-\hbar\omega)}. \tag{B19}$$

The remaining steps are analogous to the derivation of the response function in the pair-fluctuation theory; the only change is that the Feynman excitation energies $\hbar\omega_n$ in Eq. (B16) are supplemented by self-energy corrections. This is the expected modification. Defining

$$\Omega_{mnij}(\omega)\equiv\hbar(\omega_m+\omega_n-\omega)\delta_{mi}\delta_{nj}+\delta_{mi}\Sigma_{nj}^{(0)}(\hbar\omega-\hbar\omega_i)$$
$$+\delta_{mj}\Sigma_{mi}^{(0)}(\hbar\omega-\hbar\omega_j) \tag{B20}$$

and

$$\Sigma_{mn}^{(1)}(\hbar\omega)=\frac{1}{2}\sum_{ijkl}V_{ij}^{(n)}\Omega_{ijkl}^{-1}V_{kl}^{(m)}, \tag{B21}$$

we can express the pair fluctuations in terms of the one-body fluctuations

$$\sum_{mn}V_{mn}^{(i)}\delta v_{mn}^{(2)}=\sum_i\Sigma_{ik}^{(1)}(\hbar\omega)\delta v_k^{(1)}. \tag{B22}$$

Following the derivation of Ref. [42], the density-density response function is finally expressed as

$$\chi(\mathbf{r},\mathbf{r}',\hbar\omega)=\sum_{s,t}\delta\rho_1^{(s)}(\mathbf{r})[G_{st}(\hbar\omega)+G_{st}(-\hbar\omega)]\delta\rho_1^{(t)}(\mathbf{r}'), \tag{B23}$$

where the

$$\delta\rho_1^{(s)}(\mathbf{r})\equiv\tfrac{1}{2}\sqrt{\rho(\mathbf{r})}\phi_s(\mathbf{r}) \tag{B24}$$

are the Feynman density fluctuations, and

$$G_{st}(\hbar\omega)=\left[\hbar(\omega-\omega_t+i\epsilon)\delta_{st}+\Sigma_{st}^{(1)}(\hbar\omega)\right]^{-1} \tag{B25}$$

is the phonon propagator.

Attention is now directed to the fact that we have no self-energy corrections in $\Sigma_{mn}^{(0)}(\hbar\omega)$; these are present in $\Sigma_{mn}^{(1)}(\hbar\omega)$. The reason for this is evidently the restriction to triplet fluctuations; one expects that one obtains similar corrections in the three-body propagator if higher-order fluctuations are included. Anticipating such higher-order terms, we identify from now on these two self-energy corrections and consider our equations as an iterative procedure to obtain the self-energy. Thus, we shall from here on omit the superscripts (0) or (1) on the self-energy in Eq. (4.10).

[1] L. V. Hove, Phys. Rev. **95**, 249 (1954).

[2] H. Glyde, *Excitations in Liquid and Solid Helium* (Oxford University Press, Oxford, 1994).

[3] A. Griffin, *Excitations in a Bose-Condensed Liquid* (Cambridge University Press, Cambridge, 1993).

[4] C. E. Campbell and E. Krotscheck, Phys. Rev. B **80**, 174501 (2009).

[5] F. Caupin, J. Boronat, and K. H. Andersen, J. Low Temp. Phys. **152**, 108 (2008).

[6] A. R. Sakhel and H. R. Glyde, Phys. Rev. B **70**, 144511 (2004).

[7] J. V. Pearce, R. T. Azuah, B. Fåk, A. R. Sakhel, H. R. Glyde, and W. G. Stirling, J. Phys.: Condens. Matter **13**, 4421 (2001).

[8] M. R. Gibbs, K. H. Andersen, W. G. Stirling, and H. Schober, J. Phys.: Condens. Matter **11**, 603 (1999).

[9] H. R. Glyde, M. R. Gibbs, W. G. Stirling, and M. A. Adams, Europhys. Lett. **43**, 422 (1998).

[10] K. H. Andersen, W. G. Stirling, R. Scherm, A. Stunault, B. Fåk, H. Godfrin, and A. J. Dianoux, J. Phys.: Condens. Matter **6**, 821 (1994).

[11] J. Szwabiński and M. Weyrauch, Phys. Rev. B **64**, 184512 (2001).

[12] F. Pistolesi, Phys. Rev. Lett. **81**, 397 (1998).

[13] F. Pistolesi, J. Low Temp. Phys. **113**, 597 (1998).

[14] B. Fåk and J. Bossy, J. Low Temp. Phys. **112**, 1 (1998).

[15] S. Moroni, D. E. Galli, S. Fantoni, and L. Reatto, Phys. Rev. B **58**, 909 (1998).

[16] J. Boronat and J. Casulleras, Europhys. Lett. **38**, 291 (1997).

[17] M. Nava, D. E. Galli, S. Moroni, and E. Vitali, Phys. Rev. B **87**, 144506 (2013).

[18] E. Vitali, M. Rossi, L. Reatto, and D. E. Galli, Phys. Rev. B **82**, 174510 (2010).

[19] L. P. Pitaevskii, Zh. Eksp. Theor. Fiz. **36**, 1168 (1959) [Sov. Phys. JETP **9**, 830 (1959)].

[20] D. K. Lee and F. J. Lee, Phys. Rev. B **11**, 4318 (1975).

[21] T. Lichtenegger, *The Condensate Fraction of Superfluid* ^{4}He, Master's thesis, Johannes Kepler University, Linz, 2011.

[22] A. Roggero, F. Pederiva, and G. Orlandini, Phys. Rev. B **88**, 094302 (2013).

[23] E. Feenberg, *Theory of Quantum Fluids* (Academic, New York, 1969).

[24] R. P. Feynman, Phys. Rev. **94**, 262 (1954).

[25] E. C. Svensson, V. F. Sears, A. D. B. Woods, and P. Martel, Phys. Rev. B **21**, 3638 (1980).

[26] H. N. Robkoff and R. B. Hallock, Phys. Rev. B **24**, 159 (1981).

[27] F. H. Wirth and R. B. Hallock, Phys. Rev. B **35**, 89 (1987).

[28] L. Landau, J. Phys. U.S.S.R. **11**, 91 (1947).

[29] R. A. Cowley and A. D. B. Woods, Can. J. Phys. **49**, 177 (1971).

[30] T. Keller, K. Habicht, R. Golub, and F. Mezei, Europhys. Lett **67**, 773 (2004).

[31] A. D. B. Woods and R. A. Cowley, Rep. Prog. Phys. **36**, 1135 (1973).

[32] E. Krotscheck, Phys. Rev. B **31**, 4258 (1985).

[33] M. Saarela, Phys. Rev. B **33**, 4596 (1986).

[34] B. E. Clements, E. Krotscheck, and C. J. Tymczak, Phys. Rev. B **53**, 12253 (1996).

[35] P. Kramer and M. Saraceno, *Geometry of the Time-Dependent Variational Principle in Quantum Mechanics*, Lecture Notes in Physics, Vol. 140 (Springer, Berlin, 1981).

[36] A. K. Kerman and S. E. Koonin, Ann. Phys. (NY) **100**, 332 (1976).

[37] V. Apaja, J. Halinen, V. Halonen, E. Krotscheck, and M. Saarela, Phys. Rev. B **55**, 12925 (1997).

[38] J. M. C. Chen, J. W. Clark, and D. G. Sandler, Z. Physik A **305**, 223 (1982)

[39] A. Fabrocini, S. Fantoni, and E. Krotscheck, *Introduction to Modern Methods of Quantum Many–Body Theory and their Applications*, Advances in Quantum Many–Body Theory, Vol. 7 (World Scientific, Singapore, 2002).

[40] H. M. Böhm, R. Holler, E. Krotscheck, and M. Panholzer, Phys. Rev. B **82**, 224505 (2010).

[41] T. Lichtenegger, *Spin-Density Fluctuations in liquid* ^{3}He, Ph.D. thesis, Johannes Kepler Universität Linz, 2013.

[42] V. Apaja and E. Krotscheck, in *Microscopic Approaches to Quantum Liquids in Confined Geometries*, edited by E. Krotscheck and J. Navarro (World Scientific, Singapore, 2002), pp. 205–268.

[43] H. W. Jackson and E. Feenberg, Ann. Phys. (NY) **15**, 266 (1961).

[44] H. W. Jackson and E. Feenberg, Rev. Mod. Phys. **34**, 686 (1962).

[45] H. W. Jackson, Phys. Rev. A **4**, 2386 (1971).

[46] C. C. Chang and C. E. Campbell, Phys. Rev. B **13**, 3779 (1976).

[47] C. E. Campbell, Phys. Lett. A **44**, 471 (1973).

[48] C. E. Campbell and F. J. Pinski, Nucl. Phys. A **328**, 210 (1979).

[49] J. W. Clark, Nucl. Phys. A **328**, 587 (1979).

[50] C. E. Campbell and E. Feenberg, Phys. Rev. **188**, 396 (1969).

[51] C. E. Campbell, R. Folk, and E. Krotscheck, J. Low Temp. Phys. **105**, 13 (1996).

[52] C. C. Chang and C. E. Campbell, Phys. Rev. B **15**, 4238 (1977).

[53] E. Krotscheck, Phys. Rev. B **33**, 3158 (1986).

[54] E. Krotscheck, G.-X. Qian, and W. Kohn, Phys. Rev. B **31**, 4245 (1985).

[55] B. E. Clements, J. L. Epstein, E. Krotscheck, and M. Saarela, Phys. Rev. B **48**, 7450 (1993).

[56] S. A. Chin and E. Krotscheck, Phys. Rev. B **52**, 10405 (1995).

[57] D. K. Lee and F. H. Ree, Phys. Rev. A **5**, 814 (1972).

[58] F. Y. Wu and M. K. Chien, J. Math. Phys. **11**, 1912 (1970).

[59] R. Abe, Prog. Theor. Phys. (Kyoto) **21**, 421 (1959).

[60] J. M. J. van Leeuwen, J. Groeneveld, and J. D. Boer, Physica (Amsterdam) **25**, 792 (1959).

[61] H.-W. Lai, H.-K. Sim, and C.-W. Woo, Phys. Rev. A **1**, 1536 (1970).

[62] R. A. Aziz, F. R. W. McCourt, and C. C. K. Wong, Mol. Phys. **61**, 1487 (1987).

[63] G. E. Watson, J. D. Reppy, and R. C. Richardson, Phys. Rev. **188**, 384 (1969).

[64] E. Tanaka, K. Hatakeyama, S. Noma, and T. Satoh, Cryogenics **40**, 365 (2000).

[65] J. Boronat, in *Microscopic Approaches to Quantum Liquids in Confined Geometries*, edited by E. Krotscheck and J. Navarro (World Scientific, Singapore, 2002), pp. 21–90.

[66] H. J. Maris, Phys. Rev. Lett. **66**, 45 (1991).

[67] L. Vranješ, J. Boronat, J. Casulleras, and C. Cazorla, Phys. Rev. Lett. **95**, 145302 (2005).

[68] R. Hobbiger, R. Holler, E. Krotscheck, and M. Panholzer, J. Low Temp. Phys. **169**, 350 (2012).

[69] H. N. Robkoff and R. B. Hallock, Phys. Rev. B **25**, 1572 (1982).

[70] J. Boronat and J. Casulleras, Phys. Rev. B **49**, 8920 (1994).

[71] O. W. Dietrich, E. H. Graf, C. H. Huang, and L. Passell, Phys. Rev. A **5**, 1377 (1972).

[72] W. G. Stirling, in *Excitations in Two-Dimensional and Three-Dimensional Quantum Fluids*, NATO Advanced Study Institute, Series B: Physics, Vol. 257, edited by A. F. G. Wyatt and H. J. Lauter (Plenum, New York, 1991), pp. 25–46.

[73] J. Boronat and J. Casulleras, J. Low Temp. Phys. **110**, 443 (1998).
[74] S. Moroni, D. M. Ceperley, and G. Senatore, Phys. Rev. Lett. **69**, 1837 (1992).
[75] E. Svensson, P. Martel, V. Sears, and A. Woods, Can. J. Phys. **54**, 2178 (1976).
[76] H. Godfrin (private communication).
[77] K. Beauvois, C. E. Campbell, B. Fåk, H. Godfrin, E. Krotscheck, H.-J. Lauter, T. Lichtenegger, J. Ollivier, and A. Sultan (unpublished).
[78] See Supplemental Material at http://link.aps.org/supplemental/10.1103/PhysRevB.91.184510 containing details on the analytic structure of the self-energy at mode couplings.